

RESEARCH ARTICLE

Open Access



# Cranium of *Sipalocyon externus* (Metatheria, Sparassodonta) with remarks on the paleoneurology of hathliacynids and insights into the Early Miocene sparassodonts of Patagonia, Argentina

Charlène Gaillard<sup>1\*</sup> , Analía M. Forasiepi<sup>1</sup>, Sergio D. Tarquini<sup>2</sup>, Ross D. E. MacPhee<sup>3</sup> and Sandrine Ladevèze<sup>2</sup>

## Abstract

In this contribution, we investigate two sparassodonts from the Sarmiento Formation (Colhuehuapian Age; Early Miocene) recovered at the Patagonian locality of Sacanana, Chubut Province, Argentina. The first specimen (MACN-Pv CH1911), identified as *Sipalocyon externus*, is an almost complete cranium with upper dentition. The second specimen (MACN-Pv CH40), referred to *Borhyaena macrodonta*, consists of a fragmentary rostral portion of the face with associated m3–m4. The cranium of *S. externus* was studied through  $\mu$ CT-scanning to investigate its internal anatomy and infer paleoecological aspects of olfaction and hearing. In general, the endocranial anatomy and encephalization quotient are like those of other metatherians. We report the presence of an accessory transverse diploic sinus that has not previously been described in marsupials. Elements of the nasal cavity (e.g., turbinals, ossified nasal septum, cribriform plate) of *S. externus* exhibit features that are widespread among marsupials. Sense of olfaction, as evaluated from the cribriform plate and the 3D models of the olfactory bulbs, appears to have grossly resembled that of the domestic cat, a well-researched therian proxy. The dimensions of the tympanic membrane, as estimated from the preserved ectotympanic, suggest that the optimal hearing frequency of *S. externus* would have been similar to that of extant carnivorous marsupials. In sum, our study suggests that *S. externus* was a typical small-bodied (2–3 kg) hypercarnivorous metatherian that primarily relied on vision to hunt its prey, complemented by other sensory capabilities (olfaction and hearing), in a similar manner to small felids.

**Keywords** Stem Marsupialia, Neogene, Neuroanatomy, Endocast, Sensory system

Editorial handling: Marcelo Sánchez-Villagra.

\*Correspondence:

Charlène Gaillard  
charlene.gaillard.pal@gmail.com

Full list of author information is available at the end of the article



© The Author(s) 2024. **Open Access** This article is licensed under a Creative Commons Attribution 4.0 International License, which permits use, sharing, adaptation, distribution and reproduction in any medium or format, as long as you give appropriate credit to the original author(s) and the source, provide a link to the Creative Commons licence, and indicate if changes were made. The images or other third party material in this article are included in the article's Creative Commons licence, unless indicated otherwise in a credit line to the material. If material is not included in the article's Creative Commons licence and your intended use is not permitted by statutory regulation or exceeds the permitted use, you will need to obtain permission directly from the copyright holder. To view a copy of this licence, visit <http://creativecommons.org/licenses/by/4.0/>.

## Introduction

Following the Paleogene/Neogene transition, worldwide temperatures became progressively warmer, peaking in the Middle Miocene (De Vleeschouwer et al., 2017; Westerhold et al., 2020; Zachos et al., 2001). During the Early Miocene, forested environments with patches of open, dry-tolerant vegetation prevailed in Patagonia (Barreda & Palazzesi, 2010, 2014) under warm-temperate conditions (Bellosi & Gonzalez, 2010; Bellosi et al., 2021; Bucher et al., 2021). At this time, the South American land-mammal fauna was highly endemized, as a consequence of long-term biogeographical isolation (e.g., Simpson, 1980). In particular, the carnivorous mammal guild was exclusively represented by Sparassodonta, a metatherian clade related to crown Marsupialia (Suárez et al., 2023 and references therein). Sparassodonts occupied a variety of ecological niches represented by small- to large-sized predators (e.g., Prevosti & Forasiepi, 2018 and references herein).

In Patagonia, Early Miocene (Aquitanian) mammalian diversity is well represented at outcrops of the Sarmiento, Chichinales, Cerro Bandera, and Sierra Negra formations in Río Negro, Neuquén, and Chubut provinces in Argentina (Barrio et al., 1989; Garrido et al., 2012; Kramarz et al., 2005), and part of the Cura Mallín Formation in Chile (e.g., Flynn et al., 2008). One of the most productive and well-studied units of this age is the Colhue Huapi Member of the Sarmiento Formation exposed at Gran Barranca, south-central Chubut province (e.g., Madden et al., 2010). Its mammal component forms the taxonomic base for the Colhuehuapian Age

(Kay et al., 1999; Madden et al., 2010; Simpson, 1940). Radiometric dates and magnetostratigraphic studies of Gran Barranca establish that the Colhuehuapian Land Mammal Age lies between 21.0 and 20.5 Ma (Dunn et al., 2013).

The Sacanana fossil site, in north-central Patagonia (Fig. 1), is about 30 km west of the town of Gan Gan, Gastre Department, Chubut Province (e.g., Rusconi, 1933, 1935a). The site lies in the Pampa de Gan Gan and consists of outcrops of the Sarmiento Formation (Bown & Fleagle, 1993). The exposed sedimentary sequence corresponds to fluviially reworked pyroclastic deposits, intercalated with basaltic extrusive volcanic rocks (Bown & Fleagle, 1993). The sequence includes immature paleosols that are characterized by intense bioturbation, rhizoliths, and abundant invertebrate and vertebrate fossils. Stratigraphic structures in fossil-bearing levels at Sacanana suggest that the vertebrate accumulation was a consequence of quicksand entrapment (Bown & Fleagle, 1993). Like various important fossil sites in Patagonia (e.g., Madden et al., 2010), detailed geological studies at Pampa de Gan Gan are still needed.

Sacanana is known for its rich fossiliferous layers first described by C. Rusconi nearly a century ago (e.g., Rusconi, 1933, 1935b). The mammalian assemblage is represented by South American native ungulates, platyrrhine primates, caviomorph rodents, and paucituberculatan metatherians (Rusconi, 1933, 1935a–c; Hershkovitz, 1974; Fleagle & Bown, 1983; Bown & Fleagle, 1993; Kay et al., 2004; Abello, 2007; Goin et al.,



**Fig. 1** Location of the Sacanana fossil site, Chubut Province, Argentina

2007; Kay, 2010; Vucetich et al., 2010; Arnal & Kramarz, 2011). Sparassodonts have not yet been mentioned for this site, although fossils of the borhyaenid *Acrocyon riggsi* (Sinclair, 1930) have been recovered not far from Sacanana, in exposures of the Sarmiento Formation in the vicinity of provincial Route 59, between Sacanana and the Escorial (Goin et al., 2007). Overall, the taxic content of Sacanana is largely consistent with other Colhuehuapian faunas; the few taxonomic differences with Gran Barranca can be ascribed to differences in local environments (Vucetich et al., 2010).

Most of the previously collected Sacanana material consists of fossils contained in silicified concretions. This collection, pending further study, is housed in the Museo Argentino de Ciencias Naturales “Bernardino Rivadavia” (MACN) (Martinelli A. G. pers. com., 2022). Although the quality of preservation of the fossils is exquisite, concretions make preparation hard. Fortunately, microtomography ( $\mu$ CT) solves the problem of acquiring morphological information without having to physically prepare the material. Here, we present descriptions of two sparassodonts from the Sacanana collection: MACN-Pv CH1911, an almost complete cranium with upper dentition, assigned to *Sipalocyon externus* Ameghino, 1902; and MACN-Pv CH40, a fragmentary rostral portion of the face with associated m3–m4, referred to *Borhyaena macrodonta* (Ameghino, 1902).

The main goal of this study is to contribute to knowledge of the endemic South American clade Sparassodonta by focusing on morphological, taxonomic, and paleobiological aspects of newly investigated cranial material of *S. externus* and *Borhyaena macrodonta*. Use of  $\mu$ CT scanning greatly improved the inferences we have been able to make concerning novel aspects of olfaction and hearing capabilities in hathliacynids.

## Materials and methods

The fossil material (MACN-Pv CH1911 and MACN-Pv CH40) described here was collected in the 1980s during paleontological expeditions to Patagonia jointly organized by the Museo Argentino de Ciencias Naturales “Bernardino Rivadavia” of Buenos Aires, Argentina and the State University of New York at Stony Brook, USA. These expeditions were led by M. F. Soria and J. G. Fleagle. The specimen MACN-Pv CH1911 is the most complete cranium known for *S. externus*. The specimen MACN-Pv CH40 is a highly fragmentary rostral portion of the face with partial dentition, and is referred to *Borhyaena macrodonta*. For comparative material included in this study, see Additional file 1: Table S1. Scanning of MACN-Pv CH1911 was performed on the GE Phoenix vtomex L240-180  $\mu$ CT scanner housed at the X-ray Tomography Imagery Platform AST-RX MNHN in Paris, France,

with slice thickness of 0.049 mm, at 135 kV and 300 mA. The resulting image stack consists of 1994 slices of 1084×743 pixels. The cranium of *S. gracilis* Ameghino, 1887 AMNH VP-9254 was scanned at the AMNH facility in New York, USA, for which technical information is given in Forasiepi et al. (2019). The cranium of *Sipalocyon* sp. MPM-PV 4316 was scanned on the Philips Brilliance 64 tomograph of the Equipo de Neurocirugía Endovascular Radiología Intervencionista housed at the Clínica La Sagrada Familia in Buenos Aires, Argentina, at 120 kV and 313  $\mu$ A, with slice thickness of 0.400 mm, resulting in 263 slices of 77×78 pixels. The petrosal of *Sipalocyon gracilis* MACN-A 5952 was scanned on the MicroCT Bruker SkyScan 1272 housed at the Faculty of Odontology of the University of Buenos Aires (FOUBA), Argentina, at 100 kV and 100 mA, with slice thickness of 0.016 mm, resulting in 523 slices of 824×708 pixels.

Image stacks were visualized and edited in ImageJ 1.52 (Abràmoff et al., 2004). Selected images were segmented with 3D Slicer 4.10.2 (Fedorov et al., 2012) and Mimics 17.00 (Materialise, Leuven, Belgium; conducted at the Paleontology Imaging Unit of CR2P Centre de Recherche en Paléontologie Paris, MNHN/CNRS/SU) to produce digital 3D models of osseous elements and endocranial cavities. Within the braincase endocast, cranial nerves (CN) were segmented as far as their respective exit foramina, with the exception of the facial (CNVII) and vestibulocochlear (CNVIII) nerves which were cut at the internal acoustic meatus following Macrini et al. (2007b). To avoid redundant use of the term “cast”, this term is dropped in the text and, except when noted otherwise, this convention is used throughout the subsection Braincase endocast (e.g., “olfactory bulbs” refers to “olfactory bulbs cast”; “hypophyseal fossa” refers to the “hypophyseal fossa” cast).

Tooth description follows Goin et al. (2016). The homologies of the distal lower molar structures of borhyaenids follow Forasiepi et al., (2015; for alternative interpretation see Goin et al., 2007). Nomenclature for internal and external cranial descriptions follows Wible (2003, 2022) and particular additions on Sparassodonta are from Forasiepi et al. (2019). Terminology of the nasal cavity follows Macrini (2012), Rowe et al. (2005), and Wible (2022).

Measurements on the specimens were taken with a caliper. Digital measurements were taken on the 3D models in 3D Slicer (version 4.11.20200930) and Avizo/Amira 7.1 (Zuse Institute Berlin and Visualization Sciences Group, 1995–2012). Measurements on the bony labyrinth follow Ekdale (2010, 2013), with the exception of the radius of curvature, height and width of semicircular canals, and inner ear length which follow Billet et al. (2013), Hurum (1998), Luo et al. (1995), respectively. Linear measurements of the endocast follow Macrini et al. (2007a, 2007b; see also Additional file 1: Linear Measurements). Surface of the neocortex was

calculated as the surface of the cerebral hemispheres delimited by the rhinal fissure including the dorsal sagittal sinus sulcus but excluding the transverse sinus sulcus. Volume separation of the braincase endocast follows Weisbecker et al. (2021) and Macrini et al. (2007a) for the paraflocculus cast. Total volume of the braincase endocast was converted to grams by multiplying it by 0.96 (Haight & Nelson, 1987; see also Wroe et al., 2003).

Following Bird et al. (2014), we digitally isolated the perforated area of the cribriform plate and superficially filled all foramina using 3-matics Research 13.0 (Materialise, Leuven, Belgium). To render a continuous surface, a small broken fragment of the perforated area of the cribriform plate was reconstructed ( $< 1 \text{ mm}^2$ ). The resulting number of functional olfactory receptor genes was estimated based on Bird et al. (2018).

The area of the pars tensa of the tympanic membrane was estimated as the area of a circle, the maximum diameter of which fits the maximum distance between the rostral and the caudal crura as measured along the crista tympani.

Body mass was inferred from morphological measurements and previous formulas based on total jaw length and total skull length (Myers, 2001), third upper molar (M3) length (Gordon, 2003), and inner ear length (Ekdale, 2013). The encephalization quotient (EQ) equation was given by Jerison (1973). Because the equation's parameters vary in different mammalian clades (e.g., Bertrand et al., 2019; Smaers et al., 2021), encephalization quotients were calculated following three authors (Eisenberg, 1981; Jerison, 1973; Smaers et al., 2021) and given as a range of values according to the minimum and maximum body mass estimations (see also Bertrand et al., 2020).

#### Institutional abbreviations

**AMNH VP**, American Museum of Natural History, Department of Vertebrate Paleontology, New York, NY; **FMNH P**, Field Museum of Natural History, Paleontology Collection, Chicago, IL; **MACN**, Museo Argentino de Ciencias Naturales “Bernardino Rivadavia” (MACN-A, Ameghino Collection; MACN-Pv CH, fossil vertebrate collection), Buenos Aires, Argentina; **MLP**, Museo de La Plata, Buenos Aires, Argentina; **MHNC**, Muséum national d’Histoire naturelle, Paris, France; **MPM-PV**, Museo Regional Provincial “Padre M. J. Molina”, Río Gallegos, Argentina; **MPEF-PV**, Museo Paleontológico “Edigio Feruglio”, Vertebrate Paleontology Collection, Trelew, Argentina; **YPM-VPPU**, Yale Peabody Museum, ex-collection of Princeton University, New Haven, CT.

#### Anatomical abbreviations

Capital and lowercase letters refer to upper and lower teeth, respectively: **C/c**, canine; **I/i**, incisor; **M/m**, molar; **P/p**, premolar.

#### Systematic paleontology

##### Metatheria Huxley, 1880

**Sparassodonta** Ameghino, 1894

**Hathliacynidae** Ameghino, 1894

**Sipalocyon** Ameghino, 1887

**Type species.** *Sipalocyon gracilis* Ameghino, 1887

***Sipalocyon externus*** Ameghino, 1902

(Figs. 2, 3, 4, 5, 6, 7, 8, 9, 10; Additional file 1: Figures S1–14)

**Holotype.** MACN-A 52-383, a partial left palate preserving P3–M3 and partial right palate with roots of P1, complete P2–M2, and isolated M4, fragments of skull roof, and an isolated right astragalus (Additional file 1: Figure S15) from Gran Barranca, Chubut Province, Patagonia, Argentina; Colhue Huapi Member, Sarmiento Formation, Early Miocene, Aquitanian, Colhuehuapian Age.

**Referred specimen.** MACN-Pv CH1911, almost complete cranium with partially preserved upper postcanine dentition from Sacanana, Chubut Province, Patagonia, Argentina; Sarmiento Formation, Early Miocene, Aquitanian, Colhuehuapian Age.

#### Description

The specimen MACN-Pv CH1911 is well preserved, despite some lateral deformation (Fig. 2A–C; Additional file 1: Figure S1). The cranium lacks both premaxillae, the rostral part of the nasals, most of the zygomatic arches (mostly jugals and part of squamosals), most of the pterygoids, and part of the floor of the middle ear cavity. Sutures are partly discernible. Specimen is incompletely prepared due to lithified matrix.

#### Snout

The preserved part of the snout is formed by the paired maxilla, nasal, and palatine bones. The incisive foramina are missing. The snout is slightly shorter (length from the distal border of the canine alveolus to the distal root of the M4 vs. width of palate measured between the lingual roots of M4s: 1.2%) than that of *S. gracilis* (AMNH VP-9254: 1.5%) and *Cladosictis patagonica* Ameghino, 1887 (YPM-VPPU 15170: 1.9%). In dorsal view, nasals are narrow, with some broadening at the level of the infraorbital foramen. Nasals contact the lacrimals as in other sparassodonts (Babot et al., 2002; Fig. 2; Forasiepi et al., 2006, 2015; Forasiepi, 2009), and are interposed between the frontal and maxilla in contrast to extant marsupials (with some exceptions; e.g., Beck et al., 2022; O’Leary et al., 2013; Wible, 2003). The dorsal surface of the nasals is pierced by numerous tiny foramina, likely vascular (Additional file 1: Figure S3E). Suture between nasals and frontals defines a widely open U-shape and extends

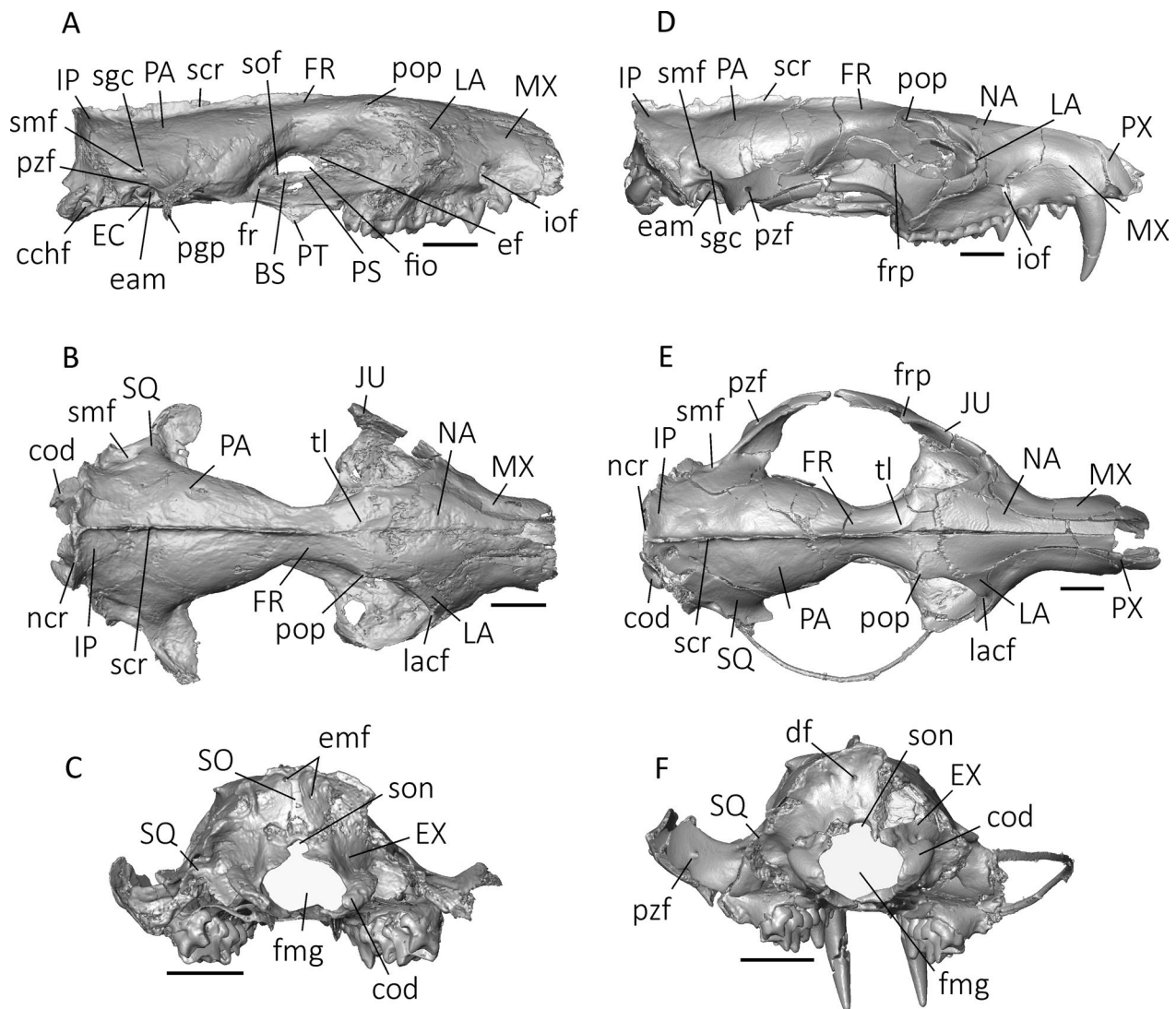


**Fig. 2** Digital reconstruction of the crania of **A–C** *S. externus* MACN-Pv CH1911 and **D–F** *S. gracilis* AMNH VP-9254 in right lateral (**A, D**), dorsal (**B, E**), and caudal (**C, F**) views. Scale bars represent 1 cm. *BS* basisphenoid, *cchf* caudal condylohyoglossal foramen, *cod* occipital condyle, *df* diploic foramen, *eam* external acoustic meatus, *EC* ectotympanic, *ef*, ethmoidal foramen, *emf* emissary foramen, *EX* exoccipital, *fio* interorbital fenestra, *fmg* foramen magnum, *FR* frontal, *fr* foramen rotundum, *frp* frontal process of the jugal, *iof* infraorbital foramen, *IP* interparietal, *JU* jugal, *LA* lacrima, *lacf* lacrima foramen, *MX* maxilla, *NA* nasal, *ncr* nuchal crest, *PA* parietal, *pggp* postglenoid process, *pop* postorbital process of frontal, *PS* presphenoid, *PT* pterygoid, *PX* premaxilla, *pzf* postzygomatic foramen, *scr* sagittal crest, *sgc* supraglenoid crest, *smf* suprameatal foramen, *SO* supraoccipital, *sof* sphenorbital fissure, *son* supraoccipital notch, *SQ* squamosal, *tl* temporal line

caudally almost to the level of the postorbital processes of the frontals, similar to the condition in *S. gracilis* (Fig. 2B, E).

In lateral view, the canine alveolus swells the facial process of the maxilla. The socket of the canine extends inside the maxilla to the level of the distal border of P2, as seen in coronal section (Additional file 1: Figure S3B). At the level of M3/M4, there is a concave area for the attachment of the superficial masseter muscle (Hiimeae & Jenkins, 1969; Turnbull, 1970). The

infraorbital foramen opens on the facial process of the maxilla (Fig. 2A). It is oval in rostral view and opens toward the rostrum at the level of the anterior root of P3, which is characteristic of most of the specimens of the genus *Sipalocyon* (Marshall, 1981; in *S. gracilis* AMNH VP-9254 the opening is slightly caudal, at mid-level of P3; Fig. 3D). The infraorbital canal is short but wide in caliber with its caudal opening, the maxillary foramen, located rostral to the level of the distal border of M1 (Fig. 3A–B). The canal transmits the infraorbital

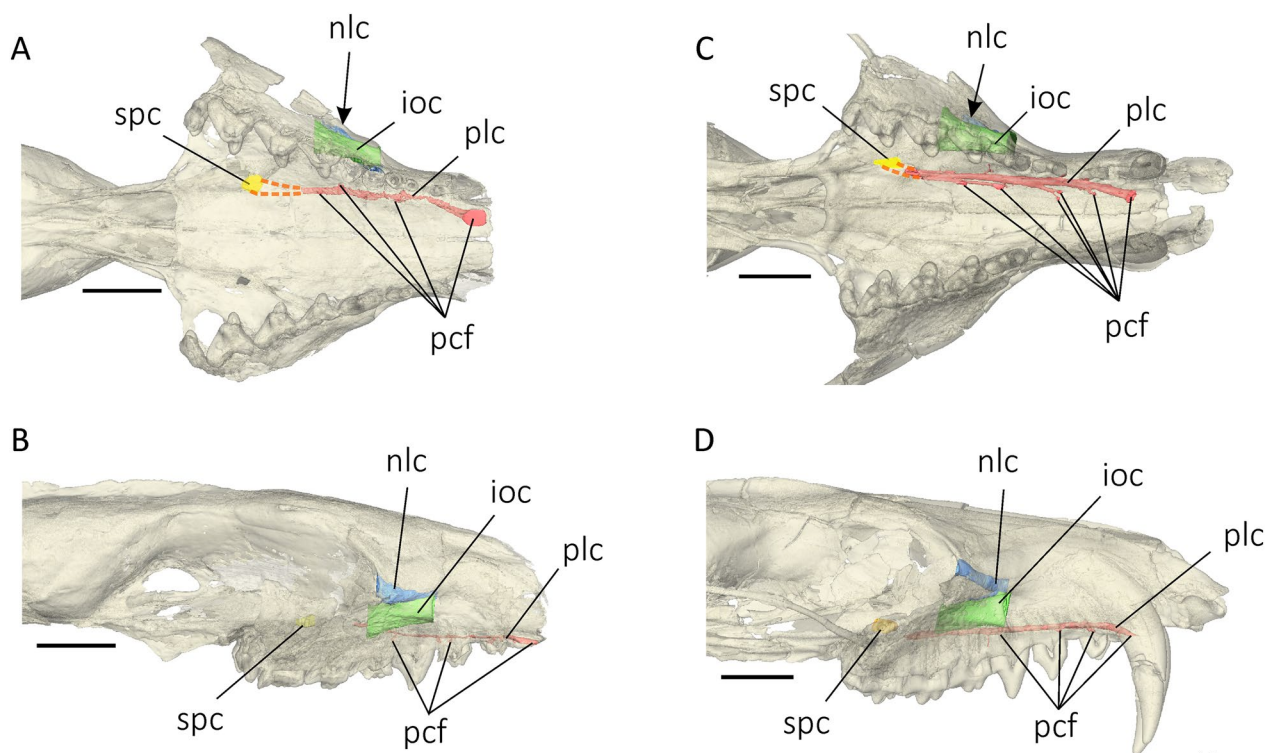


**Fig. 3** Digital reconstruction of major canals of the snout of **A, B** *S. externus* MACN-Pv CH1911 (reversed) and **C, D** *S. gracilis* AMNH VP-9254 in ventral (**A, C**) and lateral views (**B, D**). Arrows indicate the location of hidden structure. Colors: blue, nasolacrimal canal; green, infraorbital canal; red, palatine canal, orange, sphenopalatine canal. Dashed lines represent the route by which the palatine nerve reaches the pterygopalatine fossa through the sphenopalatine foramen. Scale bars represent 1 cm. *ioc* infraorbital canal, *nlc* nasolacrimal canal, *plc* palatine canal, *pcf* foramen for the palatine canal, *spc* sphenopalatine canal

nerve (CNV<sub>2</sub>) and vessels to supply the teeth, nose, face, and rhinarium (e.g., Evans & de Lahunta, 2013; Wible, 2003). In *S. gracilis*, the maxillary foramen opens at the level of the mesial root of M2 (Fig. 3C–D), more caudally than that of *S. externus*.

As seen in coronal sections, the incisivomaxillary canal extends rostrally from the infraorbital canal at the level of the mesial root of P3 near to the opening of the infraorbital foramen (Additional file 1: Figure S3C). It divides within the maxilla into smaller canals that end within the alveoli of the rostral teeth. The incisivomaxillary canal carries the rostral superior alveolar nerve of the trigeminal nerve (CNV<sub>2</sub>) and accompanying vasculature supplying the upper teeth (e.g., Archer, 1976; Evans & de Lahunta, 2013; Rowe et al., 2005).

Similar to the nasals, various tiny foramina pierce the external surface of the facial process of the maxilla, a condition seen in other sparassodonts (Forasiepi, 2009; Forasiepi et al., 2015). In ventral view, the maxilla flares outward. This feature is more evident on the left lateral side, but its appearance may be exaggerated due to lateral deformation of the cranium. The suture between the maxilla and the palatine is interdigitated. The rostral

portion of the palatine makes a circular arc concave caudally. The apex of the arc reaches the level of M1/M2 (Fig. 3A). In *S. gracilis*, the rostral portion of the palatine is rather triangular, but also reaches the level of M1/M2 (Fig. 3C). The intermaxillary suture and the mid-palatine suture are straight, with the latter slightly embossed. The hard palate extends caudally to the distal border of M4. There is no thick palatine torus, as in didelphids (e.g., Beck et al., 2022; Wible, 2003), but rather a double-arched caudal edge of the palatine. Both minor palatine foramina open at the caudal border of the palate, lateral to the nasopharyngeal passage (Additional file 1: Figure S3P). These foramina are oval and rather large. They transmit the minor palatine nerve (CNV<sub>2</sub>) and vessels to supply the soft palate (Evans & de Lahunta, 2013).

The surface of the palate is pierced by multiple small foramina on the maxilla and palatine bones (Fig. 3). Most of these foramina are irregularly distributed, except for a large pair at the level of the canines. In coronal section (Additional file 1: Figure S3A–K), these foramina as well as most of the small irregularly distributed apertures are connected by a canal of major caliber seen on both sides of the palate. This canal, identified as the palatine canal

(see below), passes through the palate inside the palatine and maxillary bones. Caudally, it runs at the level of the ethmoid plate, medial to the sphenopalatine canal, opens into the nasopharyngeal meatus, and finally terminates in the sphenopalatine foramen.

A similar pattern of foramina in the palate has been described for the extant armadillo *Euphractus sexcinctus* (Wible & Gaudin, 2004). In the dog (Evans & de Lahunta, 2013) equivalent openings are for the major palatine nerve (CNV<sub>2</sub>) and associated vasculature supplying the oral side of the hard palate. Among sparassodonts, previous interpretations based on external anatomy also considered the multiple foramina in the hard palate as openings for the major palatine nerve and accompanying vasculature (e.g., Forasiepi, 2009), given the absence of individual major openings for this structure as seen in marsupials (maxillopalatine fenestra and its synonyms in Beck et al., 2022 and references therein) and other mammals (major palatine foramen in e.g., Evans & de Lahunta, 2013). Le Verger et al. (2021) made an extensive comparison of the palatine canal and associated foramina in several xenarthrans (armadillos, including pampatheres and glyptodonts, sloths, and anteaters) and found a recurrent pattern in which confluence between the caudalmost course of the palatine and sphenopalatine canals frequently occurs among sampled species. We observed a similar canal organization in the palate of *S. externus* MACN-Pv CH1911 and *S. gracilis* AMNH VP-9254 (Fig. 3), differing from that of the dog (Evans & de Lahunta, 2013). We interpret these observations to mean that the sphenopalatine foramen of *Sipalocyon* is the route by which the palatine nerve reaches the pterygopalatine fossa (i.e., there is no individual caudal palatine foramen for the palatine canal; see also Le Verger et al., 2021).

The sphenopalatine foramen is a large aperture, located at the junction of the orbital platform and orbital wall and at the level of the anterior root of M3, similar to the condition in *S. gracilis* (Fig. 3). The sphenopalatine canal is short, connecting the pterygopalatine fossa and the nasal cavity at the level of M2. The canal conveys the caudal nasal nerve (CNV<sub>2</sub>) to supply the nasal portion of the palate, the sphenopalatine vessels (Evans & de Lahunta, 2013), and the major palatine nerve and associated vessels, as interpreted above.

### Nasal cavity

The ossified nasal septum, vomer, parts of the turbinals, and cribriform plate are mostly preserved in situ in *S. externus* MACN-Pv CH1911, providing information on a poorly known region of the cranium in fossil metatherians (Fig. 4; Additional file 1: Figures S3, 5–10). Volume of the nasal cavity is ~7000 mm<sup>3</sup> (slightly less than the

total volume of the encephalic cavity, see Braincase endocast below), with the nasopharyngeal meatus contributing ~25% of the volume and the sphenoidal recess ~75%.

The maxilloturbinal is arborlike with at least four ramifications, some of which give off other smaller branches (Fig. 4C; Additional file 1: Figures S3A, D–G, and S5). The caudalmost portion of the maxilloturbinal attaches to the lateral wall of the nasal cavity at the level of the canine root (Additional file 1: Figure S3E) and furthermore connects to the nasoturbinal at the apex of the alveolus for P3 (Additional file 1: Figure S3F). The maxilloturbinal caudally ends at the level of M1, slightly caudal to the caudalmost extent of the lateral recess (sensu Macrini, 2012; for discussion see Rossie, 2006).

The left nasoturbinal is almost completely preserved and extends along the entire nasal cavity, from the level of the canine to the cribriform plate (Fig. 4A; Additional file 1: Figures S3A–O and S6). The rostral nasoturbinal is ossified as a small but thick process similar to the one expressed in *Dromiciops gliroides* Thomas, 1894 (Macrini, 2012; Fig. 10). The rostral and caudal nasoturbinal fuse at the level of P3. The rostral part of the caudal nasoturbinal has one straight branch that occupies a large portion of the nasal cavity and is oriented laterally. Rostrally, this branch connects to the wall of the incisivomaxillary canal and caudally to that of the nasolacrimal canal (Additional file 1: Figure S3C–D). This continuous contact of the caudal nasoturbinal to other elements of the nasal cavity separates the main cavity from the space for the lateral recess (sensu Macrini, 2012). Caudal to P3, the caudal nasoturbinal loses its ventral connection to the nasolacrimal canal and occupies the dorsal part of the nasal cavity, forming an upward curl. There is one small pneumatic vacuity at the level of M2 (Additional file 1: Figure S3K), similar to that of *Dasyurus viverrinus* (Shaw, 1800) (Macrini, 2012; Figs. 9, 10). The caudal nasoturbinal also bifurcates in its rostralmost portion into a short but distinct ventral branch to which the maxilloturbinal attaches (Additional file 1: Figure S3F). This secondary branch contacts the floor of the nasal cavity caudally (Additional file 1: Figure S3H) and merges with the ethmoid plate (sensu Rowe et al., 2005).

There are five endoturbinals and two ectoturbinals (following Macrini, 2012; Fig. 4B; Additional file 1: Figures S3N–O, S7, S8). The endoturbinals and ectoturbinals are loosely packed, with few branches (Additional file 1: Figure S3L). This seems to also be the condition of *S. gracilis* based on similarly located attachment points of the endoturbinals and the ethmoid plate (Additional file 1: Figure S4F). In *S. externus*, there is a fragment of turbinal fused to the cribriform plate and other small fragments dorsal to the rostral portion of endoturbinal II that are interpreted as pieces of endoturbinal I (Fig. 4A–C). Indicia

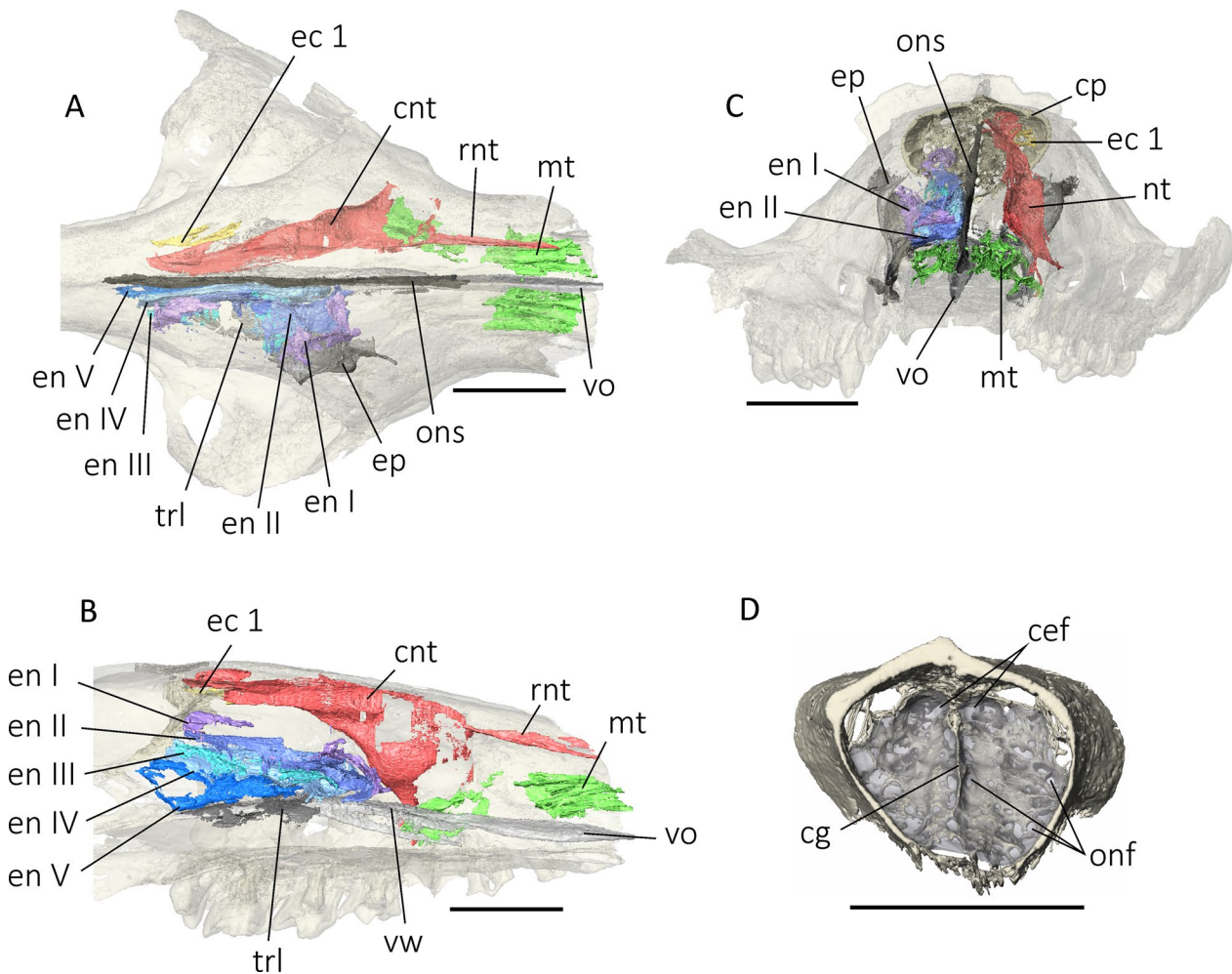


**Fig. 4** Digital reconstruction of the inner nasal bones of *S. externus* MACN-Pv CH1911 in **A** dorsal, **B** right lateral, and **C** rostral views; **D** cribriform plate in encranial view (i.e., viewed from the encephalic cavity), with wrapped surface used to estimate functional olfactory receptor genes in transparent grey. Colors: blue shades, endoturbinas; dark grey, ossified nasal septume; green, maxilloturbinal; light grey, vomer and vomerine wing; red, nasoturbinal; yellow, ectoturbinal. Scale bars represent 1 cm. *cef* cribroethmoidal foramen, *cg* crista galli, *cnt* caudal nasoturbinal, *cp* cribriform plate, *ec* ectoturbinal, *en* endoturbinal, *ep* ethmoid plate, *mt* maxilloturbinal, *onf* olfactory nerve foramen, *ons* ossified nasal septum, *rnt* rostral nasoturbinal, *trl* transverse lamina, *vo* vomer, *vw* vomerine wing

for endoturbinal I are also present on the lateral wall of the nasal cavity, where a horizontal crest indicates its original area of attachment. In addition, there is a large empty space between the nasoturbinal and endoturbinal II–V, suggesting that its volume has been partially filled by the structure of endoturbinal I (Fig. 4B). Endoturbinal I and II have small pneumatic vacuities similar to the caudal nasoturbinal (e.g., Additional file 1: Figure S3I). The ectoturbinal 1 is fragmentary but could be reconstructed, whereas ectoturbinal 2 preserved only the point of attachment to the wall of the nasal cavity (Additional file 1: Figure S3N–O).

The ethmoid plate attaches to the floor of the nasal cavity caudal to the level of M2 (Additional file 1: Figures S3L and S9). Rostrally, it attaches to the thin roof of the palatine canal. In *S. gracilis*, the ethmoid plate

attaches to the floor of the nasal cavity near the palatine canal, but apparently without fusing to it (unless breakage is obscuring the real morphology; Additional file 1: Figure S4D–E). Like the condition seen in extant marsupials (Macrini, 2012), the ethmoid plate does not contribute to the cribriform plate in *Sipalocyon*.

The lateral shelf projecting from the vomer or vomerine wing (sensu Wible, 2022) starts at the level of P3 (Additional file 1: Figure S9). This structure is similar to that of extant marsupials (e.g., *Dasyurus hallucatus* Gould, 1842). It enlarges caudally at the level of M2 to form the large and flat roof of the nasopharyngeal passage, the transverse lamina (sensu Wible, 2022). When viewed dorsally, the transverse lamina is triangular in shape with its apex caudally oriented (Additional file 1:

Figure S9). The rostral part of the transverse lamina is marked by two large notches on each side of the ossified nasal septum. The notches correspond to the caudalmost sphenethmoid apertures (Rowe et al., 2005). Rostral to them, at least two other sphenethmoid apertures are framed by the endoturbinals (Additional file 1: Figure S9). There are also three pairs of sphenethmoid apertures in *Monodelphis* Burnett, 1829 allowing the passage of air from the nasopharyngeal meatus to the olfactory epithelium of the turbinals, where neuronal interpretation takes place (Rowe et al., 2005).

The ossified nasal septum extends from the level of P2 to the cribriform plate, forming a straight and regular medial structure separating the left and right parts of the nasal cavity (Fig. 4A, C; Additional file 1: Figure S3B–P). In *S. gracilis*, the ossified nasal septum starts at the mid-level of P1 (Additional file 1: Figure S4B). The ossification of the nasal septum starts more rostrally in extant marsupials, proceeding as far as the upper canine (mesethmoid in Macrini, 2012; Rowe et al., 2005). A swelling at the base of the ossified nasal septum is present in *Sipalocyon* (Additional file 1: Figures S3B and S4B–C); it is also described for marsupials, suggesting that this swelling might be ubiquitous not only in the latter (Macrini, 2012) but in metatherians in general. There is no additional bulge in the ossified nasal septum of *S. externus*. In contrast, *S. gracilis* exhibits one long bulge extending from the level of P3 to M2 (Additional file 1: Figure S4C–E). Caudally, the ossified nasal septum connects with the cribriform plate to form the crista galli (Allen, 1882; Macrini, 2012; Rowe et al., 2005).

The crista galli, as seen in en cranial view (i.e., viewed from the encephalic cavity; sensu Allen, 1882; see also Macrini, 2012), is continuous with the cribriform plate and extends as a small ridge towards the encephalic cavity (Fig. 4D). The en cranial surface of the cribriform plate is heart-shaped and slightly concave. The dorsalmost and largest foramen of the cribriform plate is the cribroethmoidal foramen, bordered dorsally by the caudal nasoturbinale (Additional file 1: Figure S3N) and carrying a division of the ethmoidal nerve (Toeplitz, 1920; Wible, 2008). It is at least twice as large as the other foramina and triangular in shape. Ventral to the cribroethmoidal foramen are five pairs of oval foramina, similar in size, and aligned vertically as usual in extant marsupials (Macrini, 2012). Additional foramina of various sizes, all smaller than the cribroethmoidal foramen, are present around the six main pairs and most of them are distributed around the borders of the cribriform plate.

#### Orbitotemporal region

The orbitotemporal region comprises the large, continuous, oval depression as seen in lateral view, formed

jointly by the orbit and temporal fossae (Fig. 2A). Similar to other sparassodonts (except *Thylacosmilus atrox* Riggs, 1933; e.g., Riggs, 1934; Gaillard et al., 2023), there is no osseous postorbital bar in *S. externus*. The orbit would have been caudally delimited by the orbital ligament (Evans y de Lahunta, 2013) stretching between the low and rounded postorbital and frontal processes of the frontal and the jugal, respectively.

**Orbit.** Osseous orbital rim receives contributions from the frontal, lacrimal, and jugal, while wall and floor of the orbit are formed by the frontal, maxilla, and palatine bones (Fig. 2). Orbital orientation is characterized by three angles: convergence, verticality, and frontation (Heesy, 2005). Convergence is the degree to which the left and right orbits are oriented towards the front (Cartmill, 1970). Angle of orbital convergence is 60.7° for *S. externus* and 50.3° for *S. gracilis* (calculated as the dihedral angle between the sagittal plane and the orbital plane formed by three landmarks: orbital superior, orbital inferior, and orbital anterior; Heesy, 2004). Verticality measures orbital orientation in relation to the palate, whereas frontation measures orbital orientation in relation to the braincase (Heesy, 2005). Values are 44.6° and 26.3°, respectively, for *S. externus*, similar to those for *S. gracilis* (51.5° and 22.7°, respectively; Gaillard et al., 2023; following Heesy, 2005). Angle between the temporal fossa and the orbital plane (orbitotemporal angle in Heesy, 2005) is 156° for both *S. externus* and *S. gracilis* (Gaillard et al., 2023).

The lacrimal bone is narrow and does not extend onto the face (Fig. 2A, B). There is a blunt lacrimal tuberosity at the orbital rim and a single lacrimal foramen opening inside each orbit. The foramen leads to the nasolacrimal canal that houses the nasolacrimal duct (tear duct) for drainage of the lacrimal and Harderian glands (Rowe et al., 2005). As seen on the CT-scans, within the nasal cavity the nasolacrimal canal is separated from the maxillary recess (sensu Macrini, 2012) by the lacrimal bone (Fig. 3; Additional file 1: Figure S3J). Rostrally, the canal continues inside the maxillary bone until it opens into the nasal cavity just caudal to the infraorbital foramen. A similar condition is observed in *S. gracilis* AMNH VP-9254 (Fig. 3C–D). The postorbital processes of the frontals in *S. externus* are weak (MACN-Pv CH1911, Fig. 2B; holotype MACN-A 52-383, Additional file 1: Figure S15A) and less marked than in *Cladosictis* Ameghino, 1887 (e.g., Echarri et al., 2021; Marshall, 1981).

**Temporal fossa.** The temporal fossa constitutes a large area on the dorsolateral aspect of the cranium, its boundaries being defined by the temporal lines, the sagittal, nuchal, and supraglenoid crests, and the zygomatic arches. The fossa corresponds to the area housing the temporalis muscle (Hiemae & Jenkins, 1969; Turnbull,

1970). In *S. externus* (MACN-Pv CH1911, Fig. 2B; MACN-A 52-383, Additional file 1: Figure S15A), the temporal lines are short, subtle markings, arising from the low postorbital processes. The temporal lines conjoin immediately behind the postorbital process to form the sagittal crest. The sagittal crest is low (MACN-Pv CH1911, MACN-A 52-383), similar to that of *S. gracilis* (Fig. 2E), and of even height along its length as seen in lateral view (Fig. 2A). The hathliacynid *Cladosictis* has a higher sagittal crest (e.g., Echarri et al., 2021; Marshall, 1981; Sinclair, 1906). The nuchal crest is higher than the sagittal crest and U-shaped in caudal view (Fig. 2C), while the supraglenoid crest is low. Bones that contribute to the temporal fossa are frontals, parietals, interparietal, squamosals, and likely the jugals (as in other metatherians) but in MACN-Pv CH1911 the jugals have mostly been lost to breakage. The postorbital constriction in *S. externus* is strong. The width of the cranium at the level of the postorbital processes is narrower than the cranial vault width measured at the level of the base of the zygomatic arches, as in *S. gracilis* (Fig. 2F; Additional file 1: Table S2) but differing from most other sparassodonts, which exhibit the opposite width relationship (Forsasiepi, 2009).

In dorsal view, the suture between frontals and parietals is nearly straight while the one between parietals and interparietals is V-shaped. The interparietal is recognized as an individual triangular bone separate from the parietals that overlie it (Additional file 1: Figure S11I–J). This condition has been observed in *S. gracilis* and *C. patagonica* (Echarri et al., 2021; Forsasiepi, 2009), but in other sparassodonts (e.g., *Acyon*, borhyaenids, thylacosmilids, “proborhyaenids”; Babot et al., 2002; Forsasiepi et al., 2006; Forsasiepi et al., 2015) only one element representing the fused parietals and interparietal is observed in the caudal cranial roof, consistent with the hypothesis that the interparietal is universally present in mammals (Koyabu et al., 2012). The surface of the cranial roof has subtle scars for the attachment of the temporal musculature. There are also several irregularly distributed small apertures frequently found at the base of the sagittal and nuchal crests (see Insights on the cranial venous drainage).

The large oval suprameatal foramen (subsquamosal foramen sensu Archer, 1976) opens caudolaterally in the squamosal bone, dorsal to the suprameatal crest as in other sparassodonts (Forsasiepi, 2009; except for *Callistoe* Babot et al., 2002, where the opening is located ventrally to the suprameatal crest, Babot et al., 2002). Lateral to it, at the base of the zygomatic arch and on both sides of the cranium, there is a small aperture that we identify as the postzygomatic foramen. This foramen is separated from the postglenoid foramen by the supraglenoid

crest and communicates with the postglenoid canal via a small canal that pierces the squamosal (see section: Insight on the cranial venous drainage). In *S. gracilis* AMNH VP-9254, the postzygomatic foramen is more laterally placed than in *S. externus* MACN-Pv CH1911, rostral to the level of the postglenoid foramen and dorsal to the postglenoid process, but sharing a close connection with the postglenoid foramen (see Insight on the cranial venous drainage and also Wible, 2022). We interpret all associated structures as venous although an arterial component (postglenoid artery) passing through the postglenoid foramen cannot be excluded (e.g., present in short-tailed opossum *Monodelphis brevicaudata* (Erxleben, 1777); Wible, 2003, 2022).

**Infratemporal fossa.** The area below and medial to the zygomatic arch corresponds to the infratemporal fossa. In *S. externus* MACN-Pv CH1911, the infratemporal fossa receives contributions from the alisphenoid, frontal, palatine, pterygoids, orbitosphenoid, basisphenoid, and presphenoid. Partial sutures can be detected on the 3D model (Fig. 2A).

In the infratemporal fossa is a large oval opening or vacuity connecting the right and left infratemporal fossae, the interorbital fenestra (= sphenoidal fissure; Fig. 2A; Additional file 1: Figure S11B). This aperture is housed within the sphenoid complex, likely bounded by the orbitosphenoid rostrally and alisphenoid caudally (though sutures are not clearly defined between these bones) and floored by the presphenoid rostrally and basisphenoid caudally (suture between these two bones is transversal). In *S. gracilis* AMNH VP-9254, the interorbital fenestra is smaller in size, similar to the condition of *Cladosictis patagonica*. In non-hathliacynid sparassodonts, the fenestra seems small in *Prothylacynus patagonicus* Ameghino, 1887, tiny in *Borhyaena tuberata* Ameghino, 1887, and nonexistent in *Thylacosmilus atrox*. A more thorough investigation of this element using CT-scans is needed to ascertain its condition in different members of the group. The fenestra has been described for *Pucadelphys* Marshall and Muizon, 1988, *Andinodelphys* Marshall and Muizon, 1988, and *Allqokirus* Marshall and Muizon, 1988 among other fossil metatherians (Muizon & Ladevèze, 2020; Muizon et al., 2018). Smaller in size, the interorbital fenestra has also been detected in some living marsupials (e.g., *Monodelphis brevicaudata*; Wible, 2003; mentioned for *Metachirus* (Burmeister, 1854), *Monodelphis*, *Thylamys* Gray, 1843, *Caluromys* Allen, 1900, and *Marmosa* Gray, 1821; Muizon et al., 2018).

Caudal to the interorbital fenestra and sharing the same depression in the lateral side of the cranium is the sphenorbital fissure for the optic (CNII), oculomotor (CNIII), trochlear (CNIV), ophthalmic (CNV<sub>1</sub>), and abducens (CNVI) nerves and associated vessels (Fig. 2A

and Additional file 1: Figure S11C; see also Fig. 9B for the cast of the nerves; e.g., Wible, 2003). This is a large aperture facing rostrally and bounded by the sphenoid bone complex. At the caudo-ventral angle of the infratemporal fossa opens the foramen rotundum for the maxillary branch of the trigeminal nerve (CNV<sub>2</sub>); it is round and faces rostrally. In the rostral part of the fossa is also found the small ethmoidal foramen, opening at the level of the suture between orbitosphenoid and frontal (for further description on ethmoidal canal see section Braincase endocast).

On the floor of the infratemporal fossa and lateral to the nasopharyngeal passage there is a laterally concave crest that ends in a small process within the alisphenoid bone, likely for the attachment of pterygoid musculature (see the opossum in Turnbull, 1970). A similar structure is detectable in *S. gracilis* (AMNH VP-9254) but a more conspicuous process has been described for other borhyaenids (e.g., *Arctodictis sinclairi* Marshall, 1978; Forasiepi, 2009).

### Basicranium

The basicranial region receives contributions from the preserved squamosal, alisphenoid, basisphenoid, basioccipital, and exoccipital, in addition to the petrosal and ectotympanic. Sutures and synchondroses are mostly obliterated and thus hard to follow (Fig. 5). The basisphenoid-basioccipital synchondrosis is fused, roughly M-shaped and is transversal to the axis of the cranium. There is a subtle swelling at the level of the synchondrosis, likely for attachment of prevertebral neck muscles (e.g., longus capitis and rectus capitis ventralis; see Evans & de Lahunta, 2013; Fig. 5A). The ventral surface of the basisphenoid and basioccipital is damaged and displays various small breakages leading into intracranial spaces. We did not recognize the natural opening for the notochord canal detected in some marsupials (see MacPhee et al., 2023).

The glenoid cavity is oval and caudally limited by a tall postglenoid process (partly broken on both sides of the specimen; Fig. 5A). The glenoid cavity develops on squamosal bone territory; however, the state of preservation does not allow us to determine whether an alisphenoid contribution is present in the mid-part of the glenoid surface, as seen in some marsupials and other fossil metatherians (=glenoid process of the alisphenoid; see Wible, 2003; Muizon, 1999; Muizon et al., 2018; Muizon & Ladevèze, 2020), or whether it is absent, as in other sparassodonts (e.g., Marshall, 1979; Babot et al., 2002; Fig. 2; Forasiepi, 2009). Nor is it possible to confirm whether the squamosal contributes to the anterior floor of the middle ear cavity (=medial process of the squamosal sensu Muizon et al., 1997).

The postglenoid and posttympanic processes (both squamosal in origin) surround the external acoustic meatus, which in turn is medially delimited by the ectotympanic (Fig. 5A). The external acoustic meatus defines a wide U, rostrocaudally longer than wide. The posttympanic process is broken ventrally (Fig. 5A). It frames the caudal wall of the tympanic cavity, as usual in sparassodonts (e.g., Forasiepi et al., 2019). However, because of its preservation, it is not possible to evaluate whether this process also contributes to the caudal floor of the tympanic cavity in the form of a squamosal tympanic process as in *S. gracilis* (AMNH VP-9254; Fig. 5C) and other sparassodonts (Forasiepi et al., 2019). The floor of the tympanic cavity in *S. externus* MACN-Pv CH1911 receives contributions from the ectotympanic and the alisphenoid tympanic process rostrally. This latter process does not extend ventrally beyond the level of the basicranial keel (formed by the basisphenoid/basioccipital) and it does not completely enclose the tympanic cavity rostrally. This suggests that the floor of the tympanic cavity was completed in life by membrane (for the structure of the tympanic cavity see also Middle ear spaces). The roof of the tympanic cavity is defined by the epitympanic wings of the alisphenoid rostrally with a portion of the petrosal (broken tuberculum tympani; Fig. 5A, B; such as the condition observed in *S. gracilis*) and the squamosal caudally (see also Forasiepi et al., 2019).

The extracranial aperture of the foramen ovale lies at the rostral base of the alisphenoid tympanic process (Fig. 5A, B). Its endocranial aperture is directed slightly caudally. This canal is for the passage of the mandibular nerve (CNV<sub>3</sub>) and related vasculature (Additional file 1: Figure S11F). The aperture is ventrally bounded by a bridge built from the alisphenoid tympanic process (=anteromedial bullar lamina, sensu Pavan & Voss, 2016), separating the primary from the secondary foramen ovale (see Gaudin et al., 1996; Voss & Jansa, 2003, 2009). Medial to the foramen ovale the carotid foramen opens on the basisphenoid (see MacPhee & Forasiepi, 2022 for its ontogenetic development in marsupials). In ventral view, a deep bilateral carotid groove excavated on the lateral side of the basisphenoid leads into the carotid foramen. As detected in CT-scans, the carotid canals are short and medially directed. In endocranial view, the opening of each carotid canal is lateral to the hypophyseal fossa, as usual. In *S. externus*, the hypophyseal fossa is shallow (Fig. 5B) in contrast to the deeper fossa of *S. gracilis* (Fig. 5D; see also MacPhee et al., 2023).

In ventral view and rostral to the extracranial aperture of the right carotid canal, there is a small foramen which we interpret as the caudal opening of the pterygoid canal, for the nerve of the same name (Fig. 5A). A short portion of the canal is preserved, heading rostrally, lateral to the nasopharyngeal passage, and ventrally covered by a

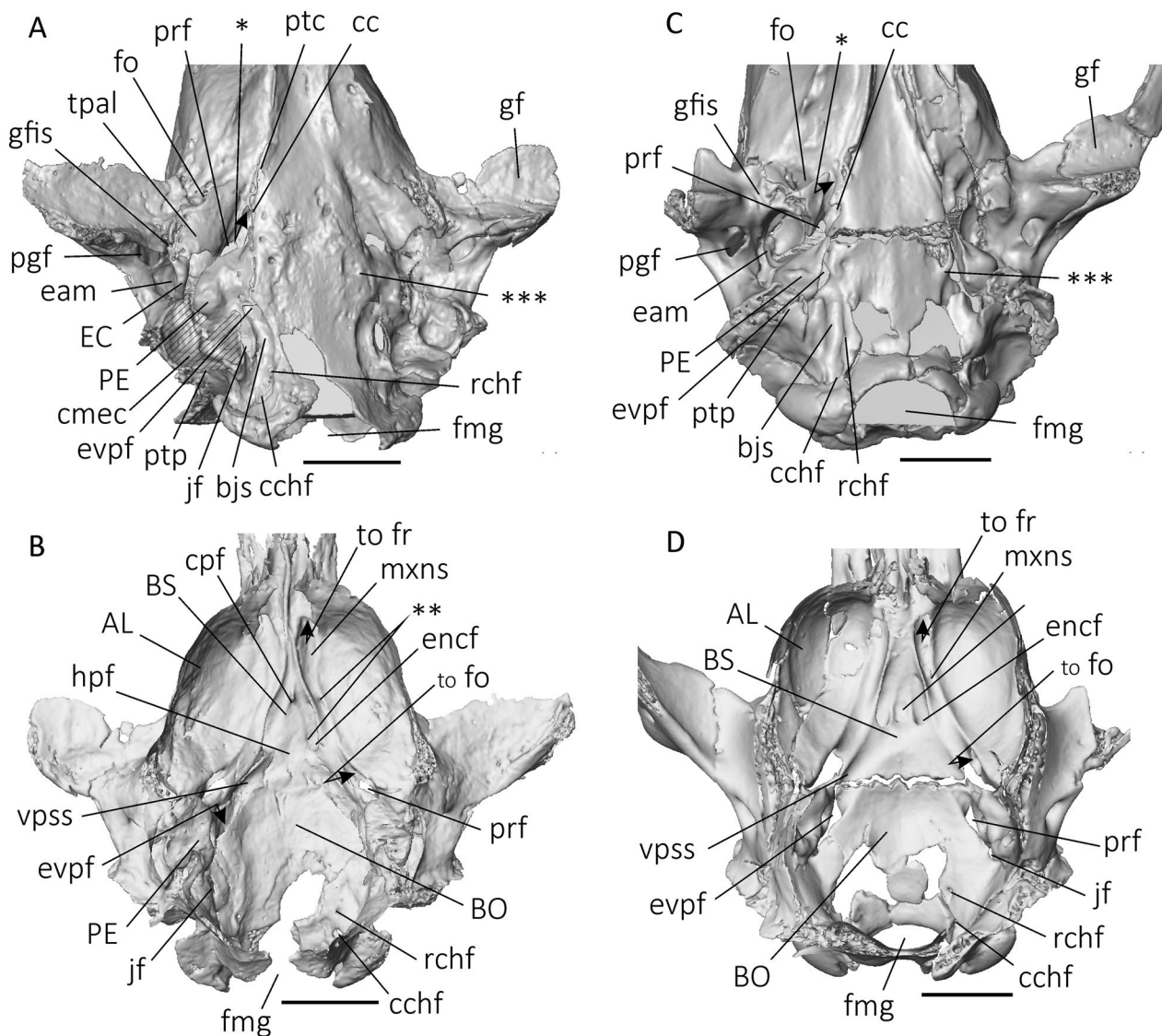


**Fig. 5** Digital reconstruction of the basicrania of **A, B** *S. externus* MACN-Pv CH1911 and **C, D** *S. gracilis* AMNHVP-9254 in right ventrolateral (**A–C**) and endocranial (**B–D**) views. Arrows indicate the location of hidden structure. Single asterisk (**A** and **C**) shows the foramen for the pterygoid canal. Double asterisks (**B**) indicate foramina connecting the rostral transverse basisphenoid sinus and the endocranial cavity floor. Triple asterisks (**A** and **B**) indicate embossment for the likely attachment of the neck muscles. Scale bars represent 2 cm. *AL* alisphenoid, *bjs* basijugular sulcus, *BO* basioccipital, *BS* basisphenoid, *cc* carotid canal, *cchf* caudal condylohypoglossal foramen, *cmec* caudal part of the middle ear space, *cpf* craniopharyngeal foramen, *eam* external acoustic meatus, *EC* ectotympanic, *encf* endocranial carotid foramen, *evpf* foramen for the external continuation of the ventral (= inferior) petrosal sinus, *fmg* foramen magnum, *fo* foramen ovale, *fr* foramen rotundum, *gf* glenoid fossa, *gfis* glaserian fissure, *hpf* hypophyseal fossa, *jf* jugular foramen, *mxns* maxillary nerve sulcus, *PE* petrosal, *pgf* postglenoid foramen, *prf* piriform fenestra, *ptc* pterygoid canal, *ptp* posttympanic process, *rchf* rostral condylohypoglossal foramen, *tpal* tympanic process of the alisphenoid, *vpss* sulcus for the ventral petrosal sinus

lamina of bone that we interpret as pterygoid in origin. In *S. gracilis* (AMNH VP-9254), the caudal opening of the pterygoid canal is more caudally located than the one of *S. externus* and can be followed until its rostral opening in the pterygopalatine fossa (Fig. 5C; see also MacPhee et al., 2023), but the canal itself has the same pattern to the one described here for *S. externus*.

Rostral to the petrosal is a small gap, the piriform fenestra, an unossified area of the basicranium that gives passage to the greater petrosal nerve (Fig. 5A, B; MacPhee, 1981). There is no separate opening for the auditory tube. Borders of the piriform fenestra on the right side of the cranium appear to be complete, but not on the left side, apparently due to breakage.

There is no transverse canal in *S. externus*, similar to the condition observed in *S. gracilis* (Fig. 5; for discussion and references concerning the transverse canal in *Sipalocyon* see MacPhee et al., 2023). As revealed by the CT scans, both rostral and caudal parts of the transverse basisphenoid sinus (tbs) are poorly developed in *S. externus*, as in *S. gracilis* (MacPhee et al., 2023). The tbs is represented by small interconnected spaces mostly restricted to the basicranial keel (Additional file 1: Figure S11E). The craniopharyngeal canal (Fig. 5B; Additional file 1: Figure S11E) opens endocranially in the rostral part of the hypophyseal fossa and connects to the rostral part of the tbs. When patent in the adult this canal is interpreted as providing venous drainage for the pituitary gland or other tissues in the rostral tbs (MacPhee et al., 2023). A small emissary foramen opens in the groove carved by the endocranial continuation of the carotid canal (endocarotid groove) and another small opening is seen at the right side of the cranium in the groove of the endocranial continuation of the maxillary nerve (Fig. 5B). These small foramina all terminate in the tbs but the location of the first foramen may suggest a likely (albeit very restricted) connection between the tbs and the internal carotid vein. Caudal to the level of the hypophyseal fossa are deep bilateral and laterally divergent grooves, the sulci for the ventral (=inferior) petrosal sinuses. Considering the large caliber of the grooves, we infer that the ventral petrosal sinus was the principal means of drainage of the cavernous sinus. There is a short intramural canal between the petrosal and basioccipital, while the foramen for the extracranial continuation of the ventral petrosal sinus lies between these two bones. The basijugular sulcus (sensu Forasiepi et al., 2019; MacPhee et al., 2023) for the external continuation of the ventral petrosal sinus defines a wide and deep groove that is concave laterally. It is excavated on the basioccipital and heads towards the condylohypoglossal foramina (sensu MacPhee et al., 2023).

There are two condylohypoglossal foramina (Fig. 5A, B). The rostral aperture is small compared to the caudal foramen whose diameter is as large as the width of the basijugular sulcus. The intracranial opening of the caudal condylohypoglossal foramen (= craniospinal foramen, sensu MacPhee et al., 2023) is of the same size as the condylohypoglossal foramen and opens at the inner border of the foramen magnum. The jugular foramen is much smaller than the craniospinal foramen (see Petrosal for jugular foramen description). The large size of the craniospinal foramen suggests that this was the principal route for drainage of the cranial cavity via the systemic circulation as in other sparassodonts and many other mammals (see Wible, 2003; Forasiepi et al., 2019; MacPhee et al.,

2023), in contrast to the derived condition (e.g., in primates) in which the internal jugular system is dominant.

### Occiput

The cranium has suffered dorsoventral crushing in this region, as is obvious in occipital view (Fig. 2C). The occiput is formed by the occipital bones and squamosal and there is no contribution from the petrosal (no mastoid exposure of the pars canalicularis) in caudal view. The foramen magnum appears oval, and the occipital condyles are flat and splayed apart. The dorsal rim of the foramen magnum contains a rounded notch (Fig. 2C; = incisura occipitalis; Voss & Jansa, 2009) slightly smaller in *S. gracilis* AMNH VP-9254 (Fig. 2F; see also Sinclair, 1906). Such a notch has been observed in almost all didelphids (Voss & Jansa, 2003, 2009) and some other mammals (O'Leary et al., 2013), for example in dogs (Kupczyńska et al., 2017), resulting from the incomplete ossification of the supraoccipital bone (e.g., Evans & Lahunta, 2013; Watson, 1981; Watson et al., 1989). The foramen magnum of didelphids possessing this notch is formed by the exoccipital and the supraoccipital (Voss & Jansa, 2009). Further study of other crania of *Sipalocyon externus* would be needed to assess the contribution of the supraoccipital to the foramen magnum.

The occiput is pierced by several small asymmetric foramina (e.g., one large on the left side of the nuchal crest close to cranial midline, and another on the right slightly more ventral in position; Fig. 2C, Additional file 1: Figure S11L). Their associated canals end in the endocranial cavity at the level of the caudal part of the vermis, where their indicia are lost. We infer that they connect to intracranial sinuses and that their major content is venous (= vv.emissaria), perhaps draining to the vascular supply of the nuchal musculature. *S. gracilis* AMNH VP-9254 also has small, irregularly distributed openings in the occiput but they terminate inside the diploe (Fig. 2F). We did not recognize a posttemporal canal (opening for arteria/vena diploetica magna) in our sample, nor for any other sparassodont taxon for which identification of this aperture is uncertain in this clade (e.g., Forasiepi et al., 2019). In didelphids the posttemporal foramen or notch (when present) usually opens at the ventrolateral margin of the occiput, between the suture of the squamosal and mastoid exposure of the petrosal (e.g., Wible, 2003).

### Middle ear

**Ectotympanic.** The right ectotympanic of *S. externus* is preserved in situ (Fig. 6A, B). Its typical U-shaped morphology closely resembles ectotympanics found in other hathliacynids (e.g., *Cladosictis patagonica*, *Acyon*

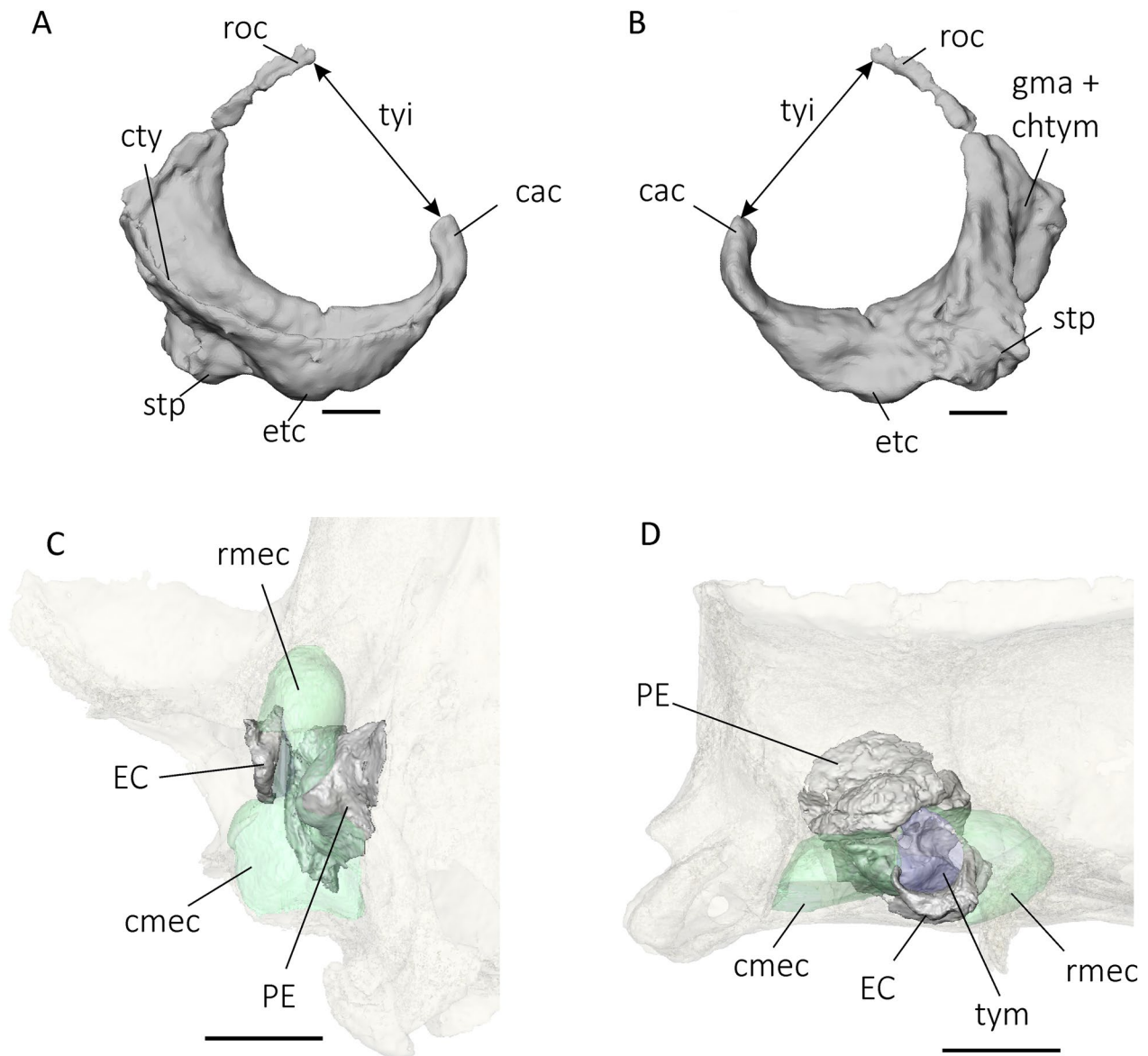


**Fig. 6** Digital reconstruction of the right ectotympanic of *S. externus* MACN-Pv CH1911 in **A** lateral and **B** medial views; **C–D** with reconstructed tympanic membrane (blue), middle ear pneumaticity (green), and petrosal (grey) in ventral (**C**) and lateral (**D**) views. Upper and lower scale bars represent 2 mm and 2 cm, respectively. *cac* caudal crus, *chtym* groove for chorda tympani nerve (facial nerve), *cmec* caudal part of the middle ear space, *cty* crista tympani, *EC* ectotympanic, *etc* ectotympanic tubercle, *gma* groove for rostral process of malleus, *PE* petrosal, *rmech* rostral part of the middle ear space, *roc* rostral crus, *stp* styliiform process, *tyi* tympanic incisure, *tym* tympanic membrane (interpreted)

*myctoderos* Forasiepi et al., 2006, and *Notogale cf. mitis* (Ameghino, 1897); Muizon, 1999; Forasiepi et al., 2006; Forasiepi et al., 2019). The rostral crus attaches to the squamosal, medial to the postglenoid foramen, similar to the condition observed in *Notogale* (Muizon, 1999), extant marsupials (e.g., *Monodelphis*; Wible, 2003), and therians generally. The styliiform process is short and robust and articulates with the tympanic process of the alisphenoid. On the medial side of the styliiform process,

a marked groove is found. In other sparassodonts, this has been interpreted as a slot for the rostral process of the malleus and the chorda tympani nerve (CNVII; Forasiepi et al., 2019; see also Wible, 2008: Fig. 25). The glaserian fissure is bordered mostly by the squamosal and the styliiform process of the ectotympanic. There is only one tubercle on the ectotympanic, rostral to the styliiform process and directed ventrally, thus differing from *Cladosictis* with three small tubercles on the

caudal crus (Forasiepi et al., 2019). The crista tympani is well defined and runs along the entire medial side of the ectotympanic. At 3.2 mm, the tympanic incisure is as wide as that of *Cladosictis* (3 mm; Forasiepi et al., 2019) but the maximum distance between the rostral and caudal crus is 4.7 mm. The caudal crus does not touch the squamosal, although this is probably due to preservation. The caudal crus of the ectotympanic of sparassodonts usually contacts the posttympanic process of the squamosal, unlike marsupials (e.g., *Mono delphis*), in which the caudal crus contacts the rostral tympanic process of petrosal (e.g., Wible, 2003).

**Middle ear spaces.** Pneumatization of the middle ear is large (at least 180 mm<sup>3</sup>; Fig. 6C, D). There is no evidence of bony segmentation (= septa) or divisions within the cavity. Rostral to the fenestra vestibuli of the petrosal, the middle ear space is enclosed by the alisphenoid tympanic process and shaped into an elongated oval of 100 mm<sup>2</sup>. Caudally, the middle ear cavity (referred to here as the cavum tympani and associated paratympanic spaces) is rectangular in shape (Fig. 6C). Because its floor is incompletely ossified in hathliacynids (supposed to be partially closed by membrane during lifetime) and is also damaged, its complete ventral extent cannot be determined. For quantitative purposes, the floor of the caudal part of the middle ear cavity in MACN-Pv CH1911 was reconstructed as the horizontal plane that contacts the squamosal, exoccipital, and petrosal, thereby closing the ventrocaudal section of the middle ear cavity. The caudal part of the middle ear cavity adds at least 80 mm<sup>3</sup> to the total volume of the middle ear cavity (Figs. 5A and 6D). Such an expanded middle ear space is not frequently described for sparassodonts, with the exception of the species *Thylacosmilus atrox*, in which this auditory region is fully ossified and extensive (depending on specimen size; Forasiepi et al., 2019).

### Petrosal

The left petrosal of *S. externus* MACN-Pv CH1911 is broken at the promontorium, but the right petrosal is complete, albeit compressed dorsoventrally (Fig. 7A–B). There is no substantial contribution of the petrosal to the floor of the auditory cavity; the rostral tympanic process of the petrosal is low, a condition also present in other sparassodonts (Forasiepi, 2009; Forasiepi et al., 2019; Muizon et al., 2018). In contrast, the contribution of the petrosal to the roof of the auditory cavity in the form of the broken tuberculum tympani is notable (Fig. 7A, C). The lateral part of pars canalicularis is not exposed in occipital aspect as in other sparassodonts (e.g., see also Muizon et al., 2018; Forasiepi et al., 2019). The petrosal

of *S. externus* contacts the squamosal laterally, the alisphenoid rostrally, the basioccipital medially, and, as inferred from by comparisons with other metatherians, the exoccipital caudally (synchondroses between occipital elements are no longer evident, e.g., Wible, 2003). The petrosal extends rostrally to the level of the basisphenoid-basioccipital synchondrosis. The ectotympanic in our 3D reconstruction is separated from the petrosal by a small distance (~ 1.5 mm). Although postmortem displacement cannot be rejected, there seems to be no bony contact between the ectotympanic and petrosal in *S. externus* (ectotympanic not preserved in *S. gracilis* AMNH VP-9254 or our comparative sample).

In tympanic view the promontorium of *S. externus* is rounded (Fig. 7A). The fossula fenestrae cochleae (=diverticulum leading to the fenestra cochleae) opens caudal to the promontorium. It is round and large, similar in size to the fenestra vestibuli. The fenestra vestibuli is 1.2 mm distant from the fossula fenestrae cochleae and has a stapedia ratio of 1.47 (width=0.72 mm, length=1.06 mm), slightly smaller than the measurements taken on the footplate of the stapes of *S. gracilis* (1.61–1.64; Gaillard et al., 2021). The tensor tympani fossa is not clearly marked on the surface of the petrosal of *S. externus* because of the poor preservation of the local bone. In contrast, in *S. gracilis* there is a shallow depression lateral to the promontorium, interpreted here as the tensor tympani fossa (Fig. 7C; see also Forasiepi et al., 2019). The secondary facial foramen is round and leads to the deep facial sulcus.

The conformation of the prootic canal in *S. externus* is difficult to ascertain. There is a small foramen on the surface of the groove for the prootic sinus, directed into the adjacent bone, but the area is fractured, making it difficult to be sure that the ostensible aperture is associated with an opening for the lateral head vein. In *S. gracilis* AMNH VP-9254 and MACN-A 5952, the prootic canal is easier to identify: there is an internal canal connecting a foramen on the surface of the prootic sinus to an extracranial aperture close to the border of the secondary facial foramen (Fig. 7C) (Forasiepi et al., 2019; Muizon et al., 2018).

The stapedia fossa of *S. externus* is a deep depression caudal to the fossula fenestrae cochleae. In *S. gracilis*, it is slightly deeper, but differences in the preservation of the petrosals are likely obscuring the real morphology (Fig. 7A, C). The anteromedial flange of the petrosal of *S. externus* is carved by the internal carotid artery sulcus that follows the rostral side of the petrosal medially to the promontorium. This sulcus can be traced where it continues rostrally into the carotid canal (located on

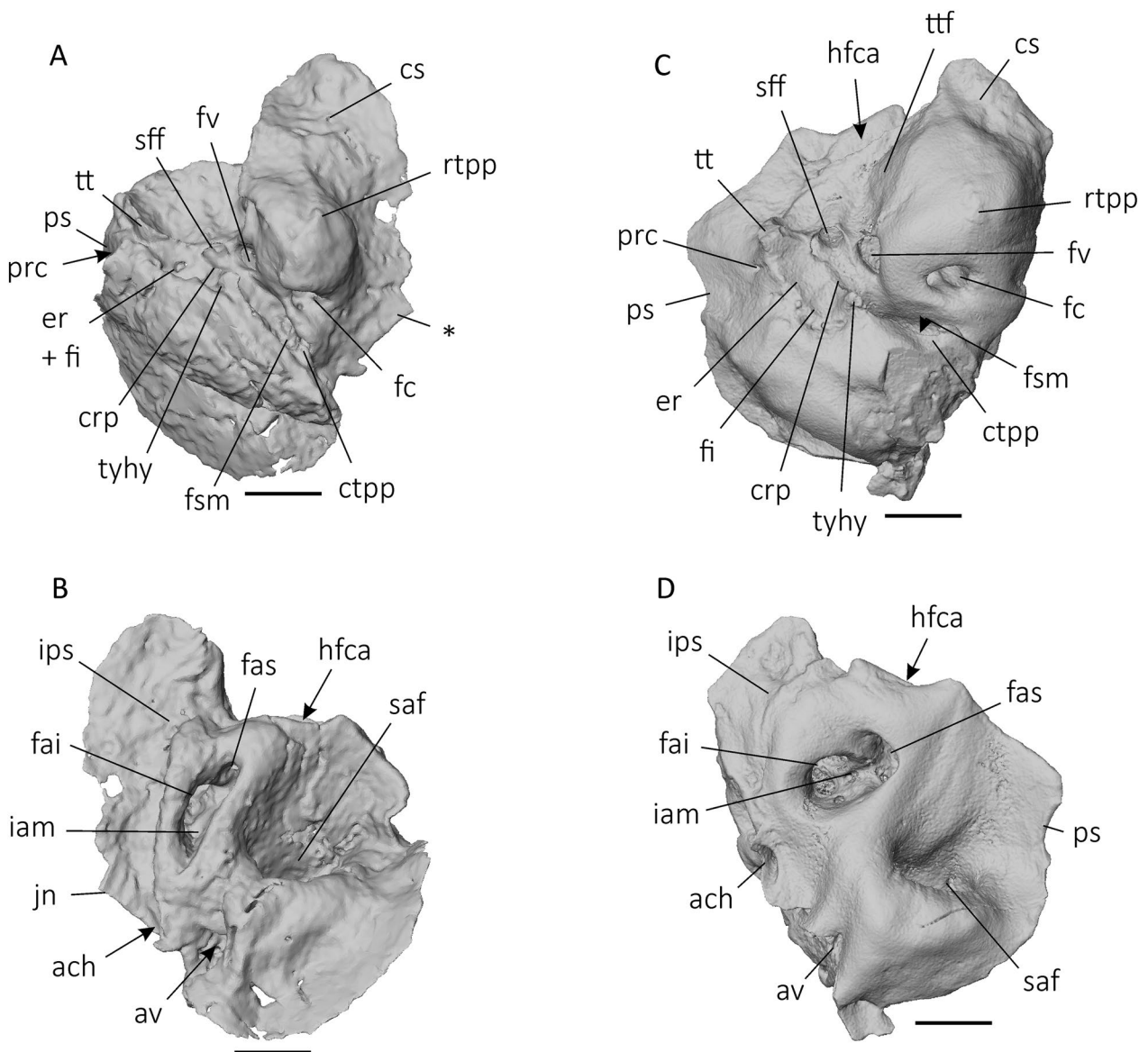


**Fig. 7** Digital reconstruction of the right petrosal of **A–B** *S. externus* MACN-Pv CH1911 and **C–D** *S. gracilis* MACN-A 5952 in tympanic (**A, C**) and cerebellar (**B, D**) view. Arrows indicate the location of hidden structures. In **A**, asterisk shows the petrosal contribution to the primary jugular foramen. Scale bars represent 2 mm. *ach* aqueductus cochlear, *av* aqueductus vestibule, *crp* crista parotica, *cs* carotid sulcus, *ctpp* caudal tympanic process of the petrosal, *er* epitympanic recess, *fai* foramen acousticum inferior, *fas* foramen acousticum superior, *fc* fossula fenestrae cochleae (=entrance to fenestra cochleae), *fi* fossa incudes, *fsm* fossa for stapedius muscle, *fv* fenestra vestibuli, *hfca* hiatus Fallopii, *iam* internal acoustic meatus, *ips* inferior petrosal sinus, *jn* jugular notch, *prc* prootic canal, *ps* sulcus for prootic sinus, *rtp* rostral tympanic process of the petrosal, *saf* subarcuate fossa, *sff* secondary facial foramen, *tt* tegmen tympani, *ttf* tensor tympani fossa, *tyhy* tympanohyal

the basisphenoid). Dorsal to the trackway of the internal carotid artery is the wide hiatus Fallopi.

A primary jugular foramen opens medially adjacent to the floor of the tympanic cavity. It is enclosed rostrally by a smooth portion of the petrosal and caudally by a thin lamina of basioccipital or squamosal (sutures are not

visible between the two bones in that region; Fig. 7A; Additional file 1: Figure S11I). The extracranial aperture of the jugular foramen is enclosed by occipital bone (likely basioccipital) and is angled to a position slightly more caudally than the primary jugular foramen (Fig. 5A, B). A similarly enclosed canal (=jugular fissure, sensu

Forasiepi et al., 2019) was described for *Thylacosmilus atrox*. In contrast, *S. gracilis* (AMNH VP-9254) lacks a jugular fissure but there is a distinct jugular foramen enclosed by the petrosal and basioccipital.

The tuberculum tympani is broken and only the stump of its base is preserved in *S. externus* where it contributes to the rostral border of the epitympanic recess caudally and the roof of the middle ear cavity rostrally. In *S. gracilis* MACN-A 5952, the epitympanic recess can be distinguished from the fossa incudis (Fig. 7C), but the two depressions are continuous in *S. externus*, likely due to the poor preservation of the petrosal. The caudal border of the fossa incudis is delimited by the tympanohyal, a small protuberance continuous with the crista parotica. In *S. gracilis*, the tympanohyal is robust and prominent. In both species, the crista parotica is short and low. The caudal tympanic process of the petrosal forms a low process caudal to the postpromontorial sinus.

In cerebellar view, the internal acoustic meatus of *S. externus* is elongated, but this seems to be the result of deformation (Fig. 7B). In *S. gracilis* (Fig. 7D) the meatus is oval. The foramen acousticum superius and inferius can be distinguished inside the meatus, separated by a superficial septum. Ventral to the internal acoustic meatus is the foramen for the aqueductus cochleae, which is well defined compared to the aqueductus vestibuli, the latter being located caudal to the former. As in other hathiacyonids, the subarcuate fossa is deep (Forasiepi, 2009; Muizon et al., 2018; see Braincase endocast, Cerebellum). In cerebellar view, there is another sulcus representing the petrosal contribution to the walls of the canal of the ventral petrosal sinus (medially enclosed by the basioccipital). The foramen for the ventral petrosal sinus is large (larger than the jugular foramen).

### Inner ear

The bony labyrinth of mammals consists of a set of interconnected spaces within the petrosal bone, which in life contain the perilymph. In the latter a series of soft-tissue sacs and ducts are suspended, comprising the membranous labyrinth. The inferior part of the membranous labyrinth includes the cochlear duct, which houses the spiral organ of hearing, and the saccule of the vestibule, which houses receptors sensitive to linear motion (e.g., Ekdale, 2015). The superior part of the membranous labyrinth is involved in detecting rotational movement of the head, and includes the utricle of the vestibule, the semicircular ducts and ampullae, and the common crus between the anterior and posterior ducts. The membranous labyrinth generally closely conforms to its osseous container, the

bony semicircular and cochlear canals (e.g., Blanks et al., 1975; David et al., 2010; Spoor, 2003).

The right bony labyrinth of *S. externus* (MACN-Pv CH1911; Fig. 8A–C) was modeled in 3D and compared with the labyrinth of *S. gracilis* (Fig. 8D–F). The general aspect of the bony labyrinth of *S. externus* is quite similar to those reconstructed for *S. gracilis* (MACN-A 5952; AMNH VP-9254; Forasiepi et al., 2019), *Allqokirus* (Muizon et al., 2018), *Andinodelphys*, and *Pucadelphys* (Muizon & Ladevèze, 2020). The cochlea of *S. externus* completes at least two turns; however, the complete turns are difficult to approximate because the 3D model is incomplete. *S. gracilis* exhibits 2.2 cochlear turns. This is congruent with the number of cochlear turns measured in other sparassodonts (except for *Borhyaena*, 1.8 turns) and living didelphids (Ekdale, 2013; Forasiepi et al., 2019; Muizon et al., 2018; Sánchez-Villagra & Schmelzle, 2007).

The anterior semicircular canal (ASC) is the longest of the three canals and exhibits the largest area (expressed as the radius of curvature) (Additional file 1: Table S5), followed by the posterior semicircular canal (PSC) and the lateral semicircular canal (LSC). The same size relation is found in *S. gracilis* (AMNH VP-9254, MACN-A 5952), *Prothylacynus*, *Borhyaena*, *Thylacosmilus*, and *Allqokirus* (Forasiepi et al., 2019; Muizon et al., 2018). The planes of the three canals are not perpendicular: the angle between the ASC and PSC approaches 103°; between ASC and LSC 73°; and only the PSC and LSC are almost perpendicular (86°). This could be the result of a slight deformation of the fossil basicranium; in *S. gracilis* (AMNH VP-9254, MACN-A 9254) all the planes are almost perpendicular to each other, as in other sparassodonts (Muizon et al., 2018; Forasiepi et al., 2019; Additional file 1: Table S5).

The semicircular canals communicate with the utricle of the vestibule through a crus commune or separate ampullae. The anterior and posterior semicircular canals are joined to form the crus commune. The lateral and posterior semicircular canals are very close, in contact in *S. externus* but do not form a secondary crus commune. The presence of a secondary crus commune is hypothesized to be a plesiomorphic character of Mammaliaformes, independently lost in many clades (Ekdale, 2013; Ruf et al., 2009).

The spherical and elliptical recesses of the vestibule are distinguished by a constriction of the vestibule lateral to the fenestra vestibuli: the swelling of the spherical recess (for the saccule) is visible in rostral view of the labyrinth and the elliptical recess (for the utricle and semicircular ducts) is bowed slightly medially to it.

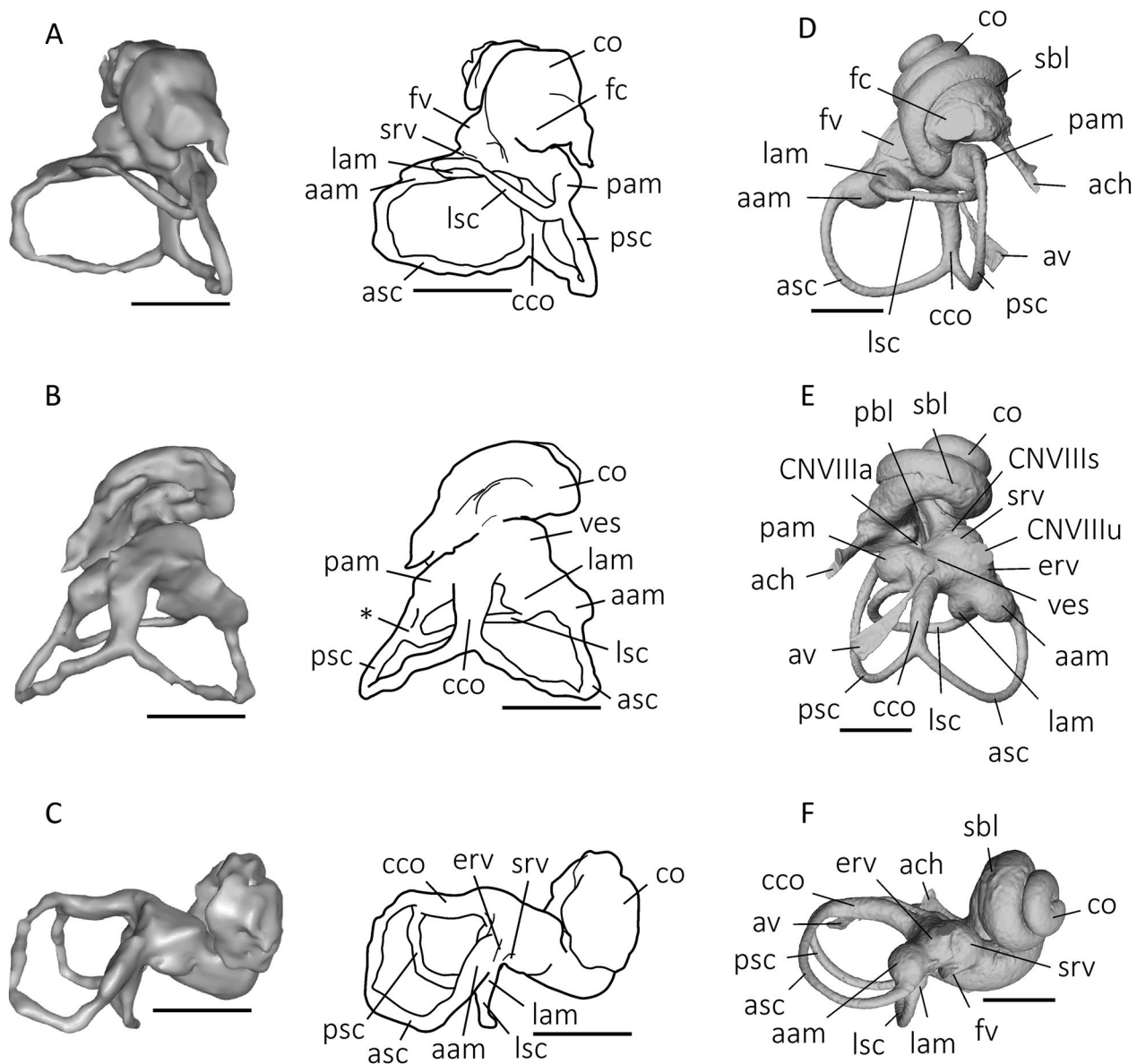


**Fig. 8** Digital reconstruction of the right bony labyrinth of **A–C** *S. externus* MACN-Pv CH1911 and **D–F** *S. gracilis* MACN-A 5952 in tympanic (**A, D**) dorsal (**B, E**), and lateral (**C, F**) views. In **B**, asterisk shows contact of the posterior and lateral semicircular canals. Scale bars represent 2 mm. *aam* anterior ampulla, *ach* aqueductus cochlear, *asc* anterior semicircular canal, *av* aqueductus vestibuli, *cco* crus commune, *CNVIII* vestibulocochlear nerve (**a** ampullar branch; **s** saccular branch; **u** utricular branch), *co* cochlea, *erv* elliptical recess of vestibule, *fc* fossula fenestrae cochleae (entrance to fenestra cochleae), *fv* fenestra vestibuli, *lam* lateral ampulla, *lsc* lateral semicircular canal, *pam* posterior ampulla, *pbl* primary bony lamina, *psc* posterior semicircular canal, *sbl* secondary bony lamina, *srv* spherical recess of vestibule, *ves* vestibule

### Braincase endocast

The braincase endocast of *S. externus* MACN-Pv CH1911 was reconstructed from the  $\mu$ CT scan (Fig. 9A–C; Additional file 1: Figure S12A–C) and compared with ones for *S. gracilis* AMNH VP-9254 (Fig. 9D–F; Additional file 1: Figure S12D–F) and *Sipalocyon* sp. MPM-PV 4316 (Additional file 1: Figure S12G–I).

The braincase endocasts of *S. externus* and *S. gracilis* are longer than wide (endocast aspect ratio of 0.47–0.48; Fig. 9). Although this relationship is found in the majority of metatherians (Macrini, 2007b), *Sipalocyon* is an outlier in having an endocast twice as long as wide (<0.5). The endocast flexures of *S. externus* and *S. gracilis* are congruent with those of extant marsupials (Macrini, 2006), but



their values are higher than those of the extinct metatherians *Pucadelphys andinus* Marshall & Muizon, 1988 (Macrini et al., 2007a) and *Andinodelphys cochabambensis* Marshall & Muizon, 1988 (Muizon & Ladevèze, 2020).

**Forebrain.** Rostrally, the braincase endocast ends in the form of multiple fiber bundles of the olfactory cranial nerve (CNI), passing through the cribriform plate (Figs. 4D and 9). Separately, the ethmoidal branch of the ophthalmic nerve (CNV<sub>1</sub>) passes through the cribroethmoidal foramen to enter the nasal cavity (Toeplitz, 1920; Wible, 2008). The division between left and right olfactory bulbs is not well defined in *S. externus*, but is better marked in *S. gracilis* and *Sipalocyon* sp. Individual olfactory bulbs are longer than wide in *S. externus* and together represent 5.8% of the total endocranial volume. This value is similar to that of *S. gracilis* and *Sipalocyon* sp., but smaller than that of *Borhyaena tuberata* (7.4%; calculated from Weisbecker et al., 2021), *Herpotherium* cf. *fugax* (10.0%; Horovitz et al., 2008), *Pucadelphys andinus* (11.7%; Macrini et al., 2007a), and *Andinodelphys cochabambensis* (12.0%; Muizon & Ladevèze, 2020). The circular fissure is deep, similar to the condition in *S. gracilis*, *Sipalocyon* sp. and all other metatherians (Forasiepi et al., 2006; Macrini, 2007a; Horovitz et al., 2008; Muizon & Ladevèze, 2020; Macrini et al., 2022).

On the ventral surface of the olfactory bulbs protrude the short ethmoidal canals (Fig. 9C). The left and right ethmoidal canals are much closer to each other in *Sipalocyon* than in other marsupials (e.g., *Didelphis virginiana* Allen, 1990, *Dasyurus hallucatus*), but conditions in other metatherians are not known. In *S. externus* and *S. gracilis*, the canals are oriented ventrorostrally, as in *Didelphis virginiana* (Wible, 2003). The ethmoidal canal carries a branch of the ophthalmic nerve (CNV<sub>1</sub>), as well as a branch of the ophthalmic artery (Archer, 1976; Wible, 2003). A swelling on the olfactory bulbs of *S. externus* (Fig. 9C) is interpreted as the sulcus for endocranial passage of the ethmoidal nerve and associated vasculature, running from the cribroethmoidal foramen to the ethmoidal foramen (Fig. 9B–C). In the dog, the ethmoidal nerve provides sensory innervation for the nasal vestibule, conchae, nasal septum (Evans & de Lahunta, 2013).

The external surface of the cerebrum cast is lissencephalic, as in *S. gracilis* (Fig. 9A, D) and most other metatherians (e.g., Forasiepi et al., 2006; Macrini et al., 2007a, 2007b; Sánchez-Villagra et al., 2007; Horovitz et al., 2008; Muizon & Ladevèze, 2020), although it differs from the endocranial cast of the borhyaenoids *Borhyaena tuberata* and *Thylacosmilus atrox* (Dozo, 1994; Quiroga & Dozo, 1988). The cast of the cerebrum of *S. externus* represents 62.6% of the total volume of the braincase endocast, similar to the percentage in *S. gracilis* (64.5%)

and *Borhyaena tuberata* (60.6%; calculated from Weisbecker et al., 2021), but less than the average for extant marsupials (70–71%; Weisbecker et al., 2021). The computed percentage of cerebrum filling the braincase endocast of *Sipalocyon* sp. is higher than that of any other metatherians (79.9%), but this figure should be treated with caution because breakage of the basicranium affects estimation of the volume of the cerebellar hemispheres. In dorsal view, the shape of the cerebrum is triangular with maximum width at the level of the transverse sinus confluence, whereas in *S. gracilis* it is oval with maximum width at the mid-length of the cerebral hemispheres. The cerebrum of *Sipalocyon* is wider than the cerebellum plus paraflocculi. The sulcus orbitalis is shallow in *S. externus* but well defined in *S. gracilis*, a condition similar to *Didelphis virginiana* (Macrini et al., 2007b). The rhinal fissure is marked on the lateral side of the cerebrum in *Sipalocyon*. Although fossil metatherians usually have no visible rhinal fissure or display only a fraction of it on the caudal cerebral hemispheres (Macrini et al., 2007a; Horovitz et al., 2008; Muizon & Ladevèze, 2020; Macrini et al., 2022), early mammals frequently have a well-defined separation of the neocortex and piriform cortex (e.g., Jerison, 1991; Kaas, 2017). A well-developed rhinal fissure was also observed in *Borhyaena tuberata* and *Thylacosmilus atrox* (Dozo, 1994; Quiroga & Dozo, 1988), suggesting a plesiomorphic condition for sparassodonts. Surface area of the neocortex of *S. externus* (delimited by the rhinal fissure) represents 46% of the total surface of the cerebrum, which is slightly smaller than the percentage of *S. gracilis* (50%).

**Midbrain.** On braincase endocasts, venous sinuses usually completely mask the midbrain in marsupials and stem metatherians (Macrini et al., 2007a, 2007b; Horovitz et al., 2008; Muizon & Ladevèze, 2020; Macrini et al., 2022), although *Thylatheridium cristatum* and *Thylophorops* cf. *chappalmalensis* are exceptions to some degree (Dozo, 1989). In *S. externus*, the sulcus of the transverse sinus can be followed from the caudal end of the neocortex, passing anterolateral to the cerebellar hemispheres until the former connects with the prootic sinus (Figs. 9, 13). The transverse sinuses are narrow until joined by the accessory transverse diploic sinus (see Insight on the cranial venous drainage), where they leave a depression between the cerebrum and cerebellum, exposing part of the midbrain (Fig. 9A). In *S. gracilis*, the transverse sinus follows the same path as in *S. externus*, also allowing midbrain exposure. The two protuberances on the depression of the midbrain are interpreted as the inferior or superior colliculi (e.g., Aitkin, 1998: Fig. 6.1 and 8.6).

**Cerebellum.** The cerebellum represents 18.3% of the total endocranial volume in *S. externus*, equivalent to that of *S. gracilis* (18.4%) but slightly larger than in *Borhyaena*

*tuberata* or the average for extant marsupials (16.2% and 14.4%, respectively, calculated from Weisbecker et al., 2021). The vermis extends laterally but poor preservation of the inner surfaces of the parietals might misrepresent its shape. In *S. gracilis*, the vermis is strongly delimited and well-rounded with a deep transversal sulcus, a feature interpreted in *Thylacosmilus atrox* as the fissura prima, separating the anterior from the posterior lobes of the cerebellum (Quiroga & Dozo, 1988). Although the vermis of *Sipalocyon* is similar in shape to that of *Thylatheridium cristatum* and *Thylophorops cf. chapalmalensis* (Dozo, 1989), it is different from the condition in *Borhyaena tuberata* and *Thylacosmilus atrox*, where it is much higher and narrower (Quiroga & Dozo, 1988). The paraflocculi of *S. externus* are ovoid, similar in shape to those of *S. gracilis*. They are not as prominent as those in some other metatherians (e.g., *Monodelphis*; Macrini et al., 2007b). On the contrary, they are almost hidden by the cerebellar hemispheres in dorsal view. The total volume of the paraflocculi corresponds to 0.23% of the endocranial volume, equal to the percentage computed in *S. gracilis*, but much less than in extant marsupials (Macrini et al., 2007b) and the fossil *Pucadelphys andinus* (Macrini et al., 2007a).

Ventrally, the hypophyseal fossa, internal carotid artery, foramen rotundum, and sphenorbital fissure are compressed medially, probably due to deformation of the cranium. The hypophyseal fossa is well defined, longer than wide and very shallow (Fig. 9B). Its size is smaller than in other metatherians (Macrini et al., 2007a, 2007b; Muizon & Ladevèze, 2020) and its volume represents a negligible percentage of the total volume of the braincase endocast. In *S. gracilis*, the hypophyseal fossa is deeper, showing better delimitation (Fig. 9E). Lateral to the caudal border of the hypophyseal fossa is the canal for the internal carotid artery. The rostral continuation of the carotid artery (ophthalmic artery) can be followed as a sulcus up to the sphenorbital fissure, where the vessel exits the encephalic cavity together with CNII–IV, V<sub>1</sub>, VI (Fig. 9, see also Fig. 5). Caudal to the internal carotid artery emerges the large ventral petrosal sinus that opens into the equally large basijugular sulcus, as already described (see also Forasiepi et al., 2019; MacPhee et al., 2023).

**Brainstem.** On the brainstem (sensu Weisbecker et al., 2021) there are two sets of canals for CNXII, here referred to as condylohypoglossal canals and foramina, following MacPhee et al. (2023). In addition to nerves, these apertures usually also contain vascular channels in therians. The caudal condylohypoglossal canal is large in *S. externus*, presumably because it also transmitted the large extracranial continuation of the ventral petrosal sinus (MacPhee et al., 2023). The brain stem in this species represents 13.6% of the encephalic volume, less than

in *Borhyaena tuberata* (15.7%; calculated from Weisbecker et al., 2021) but more than *S. gracilis* (10.3%) and the mean percentage of extant marsupials (8%; calculated from Weisbecker et al., 2021). As it is frequently the case in marsupials, the pons does not leave any indicia on the endocranial cavity of *S. externus*.

### Dentition

The upper dentition of MACN-Pv CH1911 is partially preserved (Fig. 10A). The rostral-most portion of the snout is missing, as are the incisors and canines. Only the caudal alveolar rim of the canines is preserved. The right P1–P3 series is complete, although the tips of the main cusps are broken; the left premolars are missing except for the roots of P1–P2. Both M1–M4 series are preserved but the right series is in better condition (Fig. 10A). All postcanines are completely erupted. The M4 has no wear and its crown is slightly below the crown level as defined by the other molars, suggesting that MACN-Pv CH1911 was a young adult.

The P1 is slightly oblique, rostrally deflected toward the midline. The P2–M4 series diverges distally (~30° from the palatine midline) so that the lingual distance between the left and right M4 is almost twice the distance between the left and right P2. There is a one-millimeter gap between P1–P2 and less than half-millimeter between P2 and P3. Otherwise, the teeth are mesiodistally in contact from P3 to M3.

The upper premolars are double-rooted and abruptly increase in size from P1 to P3. The crowns of the three premolars are symmetrical labiolingually but asymmetrical mesiodistally, because the main cusp of P1–P2 is shifted mesially and a distal cingulum is present. The P1 is the smallest element of the series. The main cusp is partially preserved on the right P1; its base suggests that it was asymmetrical, with its mesial face steeper than the more oblique distal face. There is no distal cuspule in P1. The P2 is also incomplete. Judging from the incompletely preserved base, the main cusp was symmetrical, with similarly inclined mesial and distal faces. There is a small and blunt distal cuspule in P2. The P3 is the tallest tooth of the postcanine tooth row. The main cusp is also symmetrical, as in P2, with a sharp crest on the distal face that connects to a distal cuspule. This latter is slightly more prominent on this tooth than on P2, and has two blunt cristae extending labially and lingually.

The molars increase in size from M1 to M3 with the latter being the largest molar. The M4 is conspicuously shorter than the other molars and slightly narrower than M3 (Additional file 1: Table S6). In M1–M3, the paracone and metacone are very close to each other, with fused bases. The metacone is taller than the paracone, increasing in size towards the M3, and accompanied by

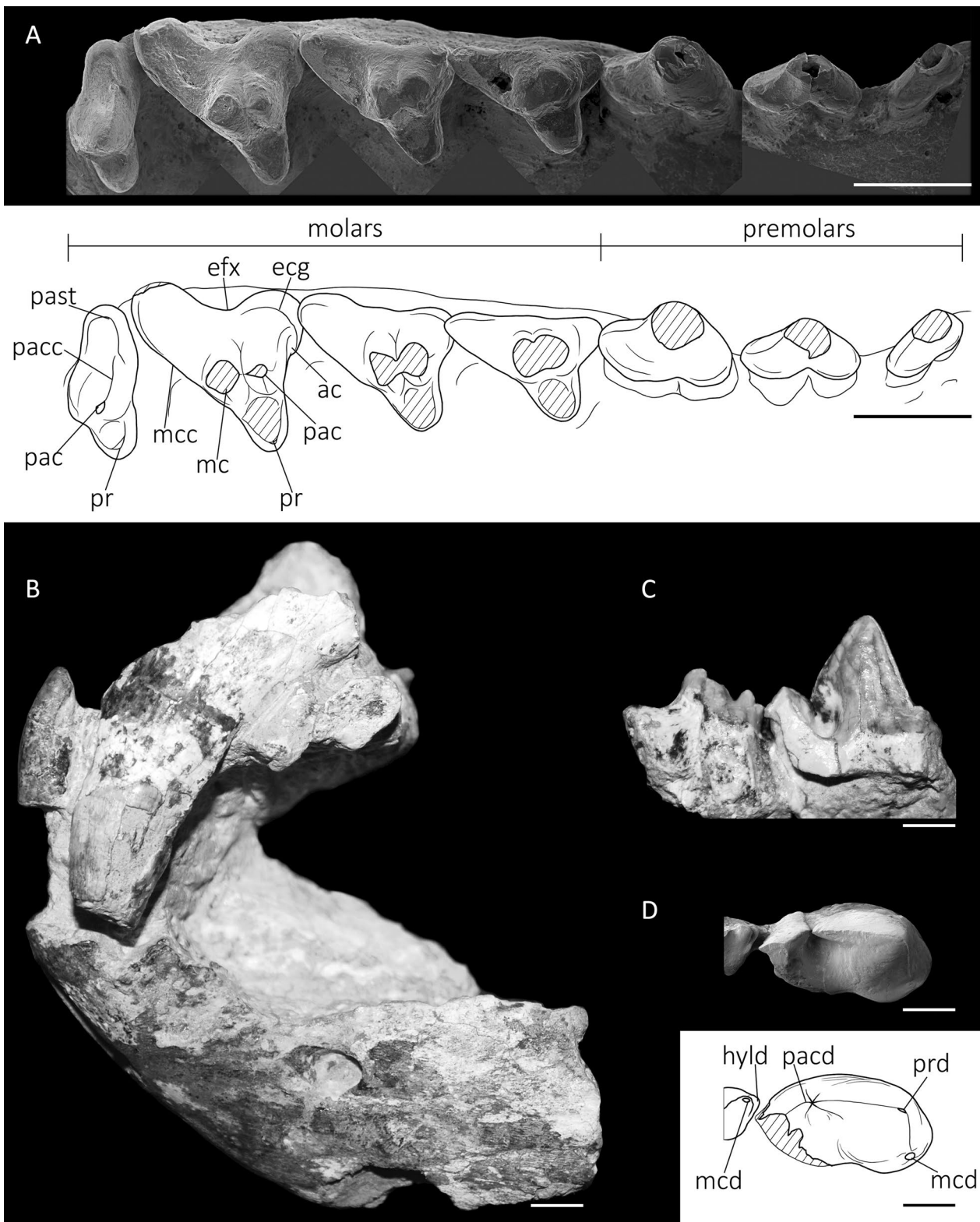


**Fig. 10** Dentition of **A** *S. externus* MACN-Pv CH1911, right upper postcanine dentition in occlusal view accompanied by line drawing, and **B–D** specimen MACN-Pv CH40 referred to *B. macrodonta*, corresponding to a fragmentary rostral portion of the face in lateral left view with upper canine and the tip of the lower canine (**B**), and a fragmentary right m3–m4 in lingual view (**C**) and occlusal view accompanied by line drawing (**D**). Scale bars represent 5 mm. *ac* anterior cingulum, *ecg* ectocingulum, *efx* ectoflexus, *hyld* hypoconulid, *mc* metacone, *mcc* postmetacrista, *mcd* metaconid, *pac* paracone, *pacc* preparacrista, *pacd* paraconid, *past* parastyle, *pr* protocone, *prd* protoconid

a long postmetacrista that also increases in length from M1 to M3. The preparacrista is obscured by wear in M1–M2; it is short in M3 and connected to the ectocingulum (see below), while it is longer in M4. The protocone is low compared to the other two cusps but lingually expanded, particularly in M3, and it is well developed in hathliacynids (e.g., more developed than in species of *Cladosictis*; Marshall, 1981). In M1–M2, the trigon basin is vestigial and partially obscured by wear. In M3 and M4, the basin is deep, broad, and delimited by two mesial and distal crests that descend from the lingual face of the paracone and metacone (M3), or paracone only (M4). Paraconule and metaconule are not observed. The styler shelf increases in size from M1 to M3. The labial border is straight in M1–M2, whereas the M3 has a deep ectoflexus defining one mesial and one distal lobe. The parastylar corner is mesially protruding in M1, while it is rounded in M2–M4. The parastyle is small in M3 as part of an ectocingulum (sensu Marshall, 1977), labial to the paracone. The anterior cingulum is short in M1–M3 and does not extend lingually from the base of the paracone.

The M4 is the smallest molar. This tooth has a tall paracone and a small protocone but lacks a metacone. There is a tiny bulge and a distal crest that descend from the distolingual border of the paracone, contributing to the border of the protocone basin, which could represent vestiges of the metacone. The trigon basin is deeper in M4 compared to the other molars, but this could be the result of lack of wear. The parastyle region is much better developed in M4 compared to other molars. In the left M4, the preparacrista is long and connected to the parastyle and paracone. However, in the right M4, there is a notch in the preparacrista, disconnecting these structures. The M4 lacks anterior cingulum (Fig. 11).

### **Borhyaenidae** Ameghino, 1894

*Borhyaena* Ameghino, 1887

**Type species.** *Borhyaena tuberata* Ameghino, 1887

*Borhyaena macrodonta* Ameghino, 1887

(Fig. 10B–D)

**Holotype.** MACN 52-390, incomplete cranium with associated right dentary and dentition (Additional file 1: Figure S16), from Gran Barranca, Chubut Province, Patagonia, Argentina; Colhue Huapi Member, Sarmiento Formation, Early Miocene, Aquitanian, Colhuehuapian Age.

**Referred specimen.** MACN-Pv CH40, fragmentary rostral portion of face, as well as associated symphyseal region of jaw, fragmentary canines, and associated m3–m4.

**Occurrence.** Sacanana, Chubut Province, Patagonia, Argentina; Sarmiento Formation, Early Miocene, Aquitanian, Colhuehuapian Age.

**Description.** The specimen MACN-Pv CH40 is not well preserved. The fragmentary face consists of a symphyseal fragment of the lower jaw with partial left lower canine, fragment of right facial part of maxilla, and incomplete left upper canine. The same concretion also contained two adjacent right lower molars (m3–m4) from the same individual.

The dentaries are unfused at symphysis. In lateral view, the anterior border of dentaries is gently curved, differing from the straighter border of other Colhuehuapian borhyaenids such as *Ar. sinclairi* (Forasiepi, 2009; Marshall, 1978) and other species (e.g., *Australohyaena antiquua* (Ameghino, 1894); Forasiepi et al., 2015). There is one mental foramen, preserved at the level of premolars, smaller than the rostralmost mental foramen of *Ar. sinclairi* MLP 85-VII-3-1.

The upper and lower canines are large but not as robust as those of *Ar. sinclairi* (Forasiepi, 2009; Marshall, 1978). There are shallow grooves at least on the accessible labial surface of the teeth, as seen in other borhyaenoids. The left lower canine preserves its apical portion, which in addition to the reduced extralveolar exposure of the root, suggests that the specimen was a young adult (see discussion in Babot et al., 2022). The m3–m4 are partially broken; minimum measurements (as the teeth are incomplete): length of m3, 13.5 mm; length of m4, 16.5 mm; and width of m4, 8.5 mm. Both molars have the protoconid as the dominant cusp followed by the paraconid. The metaconid is a very small cusp in m3 and vestigial in m4 (Fig. 10C–D). The m3 preserves some features of the talonid. The hypoconulid is caudal to the metaconid. The talonid extends as a cingular border on the medial side of the crown. On the labial side there is a postcingulid descending from the hypoconulid. The postcingulid is incomplete in m3 and highly reduced in m4. In the latter, other structure of the talonid are absent.

### **Discussion**

#### **Systematics**

**MACN-Pv CH1911.** *Sipalocyon* was a small-sized, slender hathliacynid. Following Marshall (1981), diagnostic features of the genus detected in MACN-Pv CH1911 are: large infraorbital canal, opening over anterior root of P3; supraorbital process weakly developed; dentition with small diastema, separating P1 from the upper canine and from P2; upper molars with large protocone and deeply basined trigon (sic., trigonid in Marshall, 1981); paracone and metacone fused at their base; metacone becoming larger from M1 to M3 with opposite tendency for paracone; weak but distinct parastyle in M1–M3; M4 with large paracone and protocone, lacking metacone, and paracone and parastyle connected by ridge. We observed the latter feature on

the left M4 of MACN-Pv CH1911, but on the right M4 there is a notch that disconnects the paracone and parastyle. Variability may affect the distribution of this feature. Marshall (1981) also considered diagnostic for *Sipalocyon* the presence of premolars aligned in the mediobuccal axis. In MACN-Pv CH1911, however, P1 is oblique with respect of the midline of the palate. This feature, when evaluated in a broad sample of *S. gracilis*, also suggests variability. Most frequently, P1 is parallel to the major axis of the cranium (e.g., AMNH VP-9254, MACN-A 691–703, MACN-A 5952–5953, MPM-PV 4316, YPM-VPPU 15029, YPM-VPPU 15154, YPM-VPPU 15373), but few specimens have an oblique P1 (e.g., FMNH P13777, MACN-A 5957). In the holotype of *S. externus*, MACN-A 52-383 (Additional file 1: Figure S15), P1 is almost parallel to the major axis of the cranium, differing from MACN-Pv CH1911. Similarly, Marshall (1981) considered as a diagnostic feature of *Sipalocyon* the presence of a shallow ectoflexus in M3. However, in MACN-Pv CH1911, as well as the holotype of *S. externus* MACN-A 52-383, the ectoflexus of M3 is deep, defining mesial and distal lobes. A broad sample of *S. gracilis* also shows variability with some specimens possessing shallower ectoflexus (AMNH VP-9254, MACN-A 5957, MPM-PV 4316, YPM-VPPU 15373) than others (e.g., MACN-A 691–703, MACN-A 5952–5953, YPM-VPPU 15154). In short, we conclude that some features in Marshall's (1981) diagnosis of *Sipalocyon* display variability when examined across a broad sample of specimens previously assigned to this taxon. In our analyzed sample, the holotype of *S. externus* MACN-A 52-383 and MACN-Pv CH1911 have deeper ectoflexuses than the specimens of *S. gracilis*. Finally, according to Marshall (1981), presence of distinct paraconules and metaconules is also a diagnostic feature of *Sipalocyon*. In the holotype of *S. externus*, MACN-A 52-383, the conules in M2 and paraconule in M3 are vestigial compared to the specimens of *S. gracilis*. In the M3 at the position of the metaconule, there is a crest rather than a cusp, similar to what is observed in the position of the paraconule and metaconule on the M4. In *S. gracilis* (e.g., MACN-A 691–703, MACN-A 5952–5953) para- and metaconules are visible on all upper molars. However, in MACN-Pv CH1911 the M1–M3 are greatly worn compared to the holotype of *S. externus* and conules are not observable. If they bore vestigial conules, the evidence is now lost. The M4 in turn lacks conules, similar to the holotype of *S. externus*, MACN-A 52-383.

In summary, we assign MACN-Pv CH1911 to the genus *Sipalocyon* because most of the features indicated in the diagnosis of the genus (Marshall, 1981) are present in this specimen. Although some features differ

(e.g., inclination of the P1 in relation to the cranial axis), we interpret these differences as examples of variability within the genus, as they are also seen in the holotype of *S. externus*.

Among the species of *Sipalocyon*, tooth size of MACN-Pv CH1911 agrees with that of the holotype of *S. externus* MACN-A 52-383 (Marshall, 1981: Table 7). Marshall (1981) used size as a diagnostic feature to distinguish *S. externus* from other species of the genus, but some overlap in tooth measurements occurs with the smallest specimens of *S. gracilis* (e.g., Marshall, 1981: Table 10). In other dental features, *S. externus* is closely similar to *S. gracilis* (see also Goin et al., 2007), along with subtle differences expressed by the protocone of M1 (e.g., cusp smaller in size, with a more restricted trigon basin, and a more deeply excavated ectoflexus; Marshall, 1981), features present in both the holotype of *S. externus* MACN-A 52-383 and MACN-Pv CH1911. In addition, paraconule and metaconule are vestigial in the antemolar dentition and absent in M4, as seen in the holotype of *S. externus*, the latter feature being also observed in MACN-Pv CH1911. Tooth size in combination with the features discussed herein are the basis for our taxonomic interpretation of MACN-Pv CH1911 as *S. externus*. Finally, it is worth mentioning that the M4 bears a large and basined protocone, as indicated in the original diagnosis of the genus (Marshall, 1981). The protocone on the M4 of MACN-Pv CH1911 is slightly larger than in the holotype but similar to the compared specimens of *S. gracilis* (e.g., MACN-A 691–703, MACN-A 5957–5958, MACN-A 5952–5953). In contrast, Goin et al. (2007) assigned to *S. externus* an isolated M4 (MPEF-PV 5832) that lacks a protocone, which could indicate large variability in this feature if the assignment is correct.

From the study of the CT scans of the cranial anatomy of *Sipalocyon*, we add the following features to differentiate *S. externus* from *S. gracilis*: 1. *S. externus* exhibits a primary jugular foramen closed by the petrosal and a lamina of the basioccipital, or possibly squamosal, that leads to the jugular fissure (sensu Forasiepi et al., 2019; Fig. 5A), whereas *S. gracilis* has an enclosed jugular foramen formed by the petrosal and basioccipital (Fig. 5C). 2. In *S. externus* the general morphology of the cerebral hemispheres is triangular and resembles that of *Didelphis* (Fig. 9A; Macrini et al., 2007b), whereas the cerebral hemispheres of *S. gracilis* are ovoid, resembling *Monodelphis* in this regard (Fig. 9D; Macrini et al., 2007b). 3. The accessory transverse diploic canals in *S. externus* are straight while those of *S. gracilis* are orientated rostrally, paralleling the dural transverse sinus and more rostrally the superior sagittal sinus up to the rostral part of the frontal diploe (see Insights on the cranial venous drainage). 4. *S. externus* presents pneumatization of

the squamosal in the caudal ear region, resulting in an enlarged middle ear cavity caudal to the fenestra vestibuli (Figs. 5A, 9C). The middle ear cavity of *S. gracilis* is limited to the volume floored by the tympanic process of the alisphenoid rostral to the fenestra vestibuli (Fig. 5C). These features should be tested in the context of a broader sample before adding to the diagnosis of the genus in order to avoid incorporating intraspecific variability.

**MACN-Pv CH40.** Specimen MACN-Pv CH40 is here referred to Borhyaenidae on the basis of the very reduced and vestigial talonid of the lower molars (as seen in species of *Acrocyon*, *Australohyaena*, *Arctodictis*, *Borhyaena*—see for examples Marshall, 1978; Goin et al., 2007; Forasiepi, 2009; Forasiepi et al., 2015). The size and robustness of the fragment of the dentary and teeth suggest that the close similarities are with *Borhyaena macrodonta* and *Acrocyon riggsi* (Goin et al., 2007; Marshall, 1978), known from the Early Miocene Colhuehuapian (Goin et al., 2007; Marshall, 1978).

The species *Borhyaena macrodonta* is based on an incomplete cranium with associated right dentary and dentition, MACN 52-390 (Additional file 1: Figure S16), from Gran Barranca, Colhue Huapi Member, Sarmiento Formation, Chubut, Argentina. Considering that tooth measurements provided in the description of MACN-Pv CH40 are minima because the teeth are incomplete, m3–m4 size closely approximate those of the *Borhyaena macrodonta* holotype (length of m3: 14 mm; length of m4: ca. 18 mm; Marshall, 1978: Table 4). According to Marshall (1978), larger size differentiates *Borhyaena macrodonta* from the very similar coetaneous species *Acrocyon riggsi*. In addition, the rostral portion of dentary of MACN 52-390 is gently curved and the symphysis is unfused, as in MACN-Pv CH40. Upper and lower canines are larger in the holotype of *Borhyaena macrodonta* than MACN-Pv CH40 but this could relate to the age (canines in borhyaenoids continue growing after all the molars have completed eruption; Babot et al., 2022; Forasiepi & Sánchez Villagra, 2014), in addition to sex or individual variation, as already indicated for the species (Marshall, 1978). Metacone on the m3 of MACN-Pv CH40 is slightly larger than that of the holotype, but similar to specimen MLP 92-X-10-8 (Goin et al., 2007: Fig. 7F), for which minor variation is noted.

*Acrocyon riggsi* was named on the basis of a robust skull FMNH P13433 from Gran Barranca, Colhue Huapi Member, Sarmiento Formation, Chubut, Argentina (Marshall, 1978; Sinclair, 1930). To this species Goin et al. (2007) referred an incomplete dentary with dentition (MLP 85-II-1-1), found not far from Sacanana. According to Goin et al. (2007), the inclusion of this specimen in the hypodigm of *Acrocyon riggsi* may add to the diagnosis of

the genus the presence of a crest on the distal face of the protoconid (here interpreted as a vestigial postprotocristid following homological assumptions in Forasiepi et al., 2015) and the aligned disposition of the major cusps of the lower molar (homologous to paraconid, protoconid, and metaconid as interpreted here). The first feature however seems to be more broadly distributed among borhyaenids (e.g., *Borhyaena macrodonta* MACN-A 52-390), variably present and/or sometimes obscured by wear. At least on the m4, MACN-Pv CH40 lacks a crest or thickening on the postprotocristid. Regarding the second trait, major cusps on the lower molar in MACN-Pv CH40 define an open triangle. In addition, features of the lower jaw of MLP 85-II-1-1 include deep and robust dentaries fused at the symphysis in adults (Goin et al., 2007), which differs from MACN-Pv CH40. Assuming our interpretations are correct, the large borhyaenid from Sacanana, MACN-Pv CH40, is tentatively referred to *Borhyaena macrodonta*, pending a deeper investigation of the main anatomical defining within *Borhyaena*.

#### Encephalization and braincase endocast

This study presents a 3D digital reconstruction of the braincase endocast of MACN-Pv CH1911 that notably increases the information available for Sparassodonta (Dozo, 1994; Forasiepi et al., 2019; Quiroga & Dozo, 1988; Weisbecker et al., 2021) and, more broadly, stem Marsupialia and other fossil metatherians (e.g., Dozo, 1989; Forasiepi et al., 2006; Horovitz et al., 2008; Macrini et al., 2007a; Muizon & Ladevèze, 2020; Macrini et al., 2022).

The braincase endocasts of *Sipalocyon* are similar to those of extant marsupials, but the general morphology of the two are notably different, *S. externus* being more similar to *Didelphis* and *S. gracilis* resembling more *Monodelphis*.

The lissencephalic surface of the braincase endocast of *Sipalocyon* corresponds to general trends known in didelphids, dasyurids (with the exception of *Thylacinus cynocephalus* Harris, 1808; e.g., Macrini et al., 2007b), and most fossil metatherians (Dozo, 1989; Forasiepi et al., 2006; Macrini et al., 2007a; Horovitz et al., 2008; Muizon & Ladevèze, 2020; Macrini et al., 2022), but contrasts with the gyrencephalic endocasts of the non-hathliacynid sparassodonts *Borhyaena tuberata* and *Thylacosmilus atrox* (Dozo, 1994; Quiroga & Dozo, 1988).

The olfactory bulbs of *Sipalocyon* are smaller than expected when compared to other stem marsupials (see Paleocology, Nasal structures and olfaction). The paraflocculi are also small in comparison to those of other marsupials (e.g., Macrini et al., 2007a, 2007b; Muizon & Ladevèze, 2020). Because the reconstructed volume of the paraflocculi from the subarcuate fossa may not accurately represent the true size of the paraflocculi

(Sánchez-Villagra, 2002), their small size in *Sipalocyon* only indicate that they were not enlarged relative to extant marsupials.

On the braincase endocast of *Sipalocyon*, the midbrain is visible between the cerebellar hemispheres and the cerebellum. In *S. gracilis*, the left and right protuberances of the inferior colliculi are marked, but they are not discernible in *S. externus*. In placentals, exposure of the midbrain is regarded as basal in primates and rodents (Bertrand et al., 2019; Silcox et al., 2009, 2010). In metatherians, however, Macrini (2006) reconstructed the ancestral state of the midbrain as unexposed, due to presence of the overlapping sinus. In this context, the derived condition in *Sipalocyon* (midbrain exposed) might be linked to the presence of the large accessory transverse diploic sinus, which presumably played a role in sending part of the encephalic drainage through the vessels in the parietal diploe, thereby reducing the volume passing through the (original) transverse sinus. If this resulted in smaller sinus calibers, the end result would mean greater midbrain exposure (see section Insights on the cranial venous drainage).

To summarize, the braincase endocast of *Sipalocyon*, although didelphid-like, exhibits derived states, such as exposure of midbrain and relatively small olfactory bulbs and paraflocculi.

### Paleoecology

**Body mass.** Estimated body masses for *S. externus* MACN-Pv CH1911 are as follows (Table 1 and related measurements in Additional file 1: Table S4): 2.33 kg (equation from Myers, 2001), 2.67 kg (equation from Gordon, 2003), and 1.15 kg (equation from Ekdale, 2013). Additionally, body mass estimations for *S. gracilis* AMNH VP-9254 ranges between 1.34 and 4.84 kg,

whereas values for *Sipalocyon* sp. MPM-PV 4316 are 1.31–1.87 kg.

Body mass estimation based on inner ear length is similar for both species and are the lowest estimated values. Given that Ekdale's (2013) formula was generated for mammals in general, with few metatherian exemplars included, we suggest rejecting these estimations in this case. We therefore consider the two other inferences (equations from Myers (2001) and Gordon (2003), based on living marsupials) to be more reliable and estimate the body mass range of *S. externus* MACN-Pv CH1911 at 2.3–2.7 kg, *S. gracilis* AMNH VP-9254 at 1.8–4.8 kg, and *Sipalocyon* sp. MPM-PV 4316 at 1.3–1.9 kg. The body masses for *S. gracilis* are similar to previous estimations using dental equations (1.9 kg, Vizcaíno et al., 2010; 2.0 kg, Prevosti et al., 2013; 1.8–2.7 kg, Croft et al., 2017) and postcranial measurements (1.0–5.0 kg, Argot, 2003a; 2.1 kg, Ercoli & Prevosti, 2011). We note that this is the first time that body mass inferences for *S. externus* have been made on actual material from this species; previous efforts were based on comparisons with sparassodonts of similar size (Prevosti & Forasiepi, 2018; Prevosti et al., 2013). Overall, the body mass range of *S. externus* overlaps with smaller specimens of *S. gracilis*.

**Encephalization quotient.** Encephalization quotients (EQ) for *S. externus* MACN-Pv CH1911, *S. gracilis* AMNH VP-9254, and *Sipalocyon* sp. MPM-PV 4316 have similar values (Table 1). The maximum EQ value observed in *S. gracilis* (Table 1, see also Additional file 1: Tables S3–S4) is interpreted as an artifact of the underestimated body mass of AMNH VP-9254. Following the equation of Jerison (1973), values for all three specimens are lower than the ones for the borhyaenoids *Borhyaena tuberata* and *Thylacosmilus atrox* (0.64 and 0.72–0.73, respectively; Quiroga & Dozo, 1988; Dozo, 1994), but are higher than that for the fossil metatherian *Pucadelphys andinus* (0.17–0.19; Macrini et al., 2007a). Compared

**Table 1** Estimated body weight and brain weight in grams with encephalization quotient for *Sipalocyon*

Species		<i>Sipalocyon externus</i>	<i>Sipalocyon gracilis</i>	<i>Sipalocyon</i> sp.
Collection number		MACN-Pv CH1911	AMNH VP-9254	MPM-PV 4316
Estimated body mass [g]	Min	2331	1770	1310
	Max	2670	4840	1870
Estimated brain weight [g]		7.82	11.03	5.98
	Without ob	7.32	10.38	5.65
Jerison (1973)		0.31–0.34	0.30–0.58	0.31–0.39
	Without ob	0.30–0.32	0.28–0.55	0.29–0.37
Eisenberg (1981)		0.43–0.48	0.39–0.83	0.43–0.56
	Without ob	0.41–0.45	0.37–0.78	0.41–0.53
Smaers et al. (2021)		0.65–0.70	0.65–1.16	0.61–0.75
	Without ob	0.61–0.66	0.61–1.09	0.58–0.71

max maximum value, min minimum value, ob olfactory bulbs

to extant marsupials, the EQ of *Sipalocyon* is within the range of EQs of didelphids (0.24–0.42; Macrini et al., 2007a), although it is lower than that of the extinct didelphid *Thylatheridium cristatum* Reig, 1952 (0.55; Dozo, 1989).

For comparison, following the equation of Eisenberg (1981), the EQ of *Sipalocyon* is higher than that of the fossil metatherian *Pucadelphys andinus* (0.28–0.32; Macrini et al., 2007a), but similar to extant didelphids (0.30–0.68; Macrini et al., 2007a). Following the equation of Smaers et al. (2021), the EQs of *Sipalocyon* are lower than the ones for extant marsupials, in distinction to those estimated using the equations of Jerison (1973) and Eisenberg (1981).

Viewing all three equations, it may be concluded that EQ values of *Sipalocyon* are consistently similar to or slightly lower than the ones for didelphids but higher than those for *Pucadelphys*. Among sparassodonts, *Sipalocyon* has lower encephalization than borhyaenids. In the absence of data on other hathliacynids, it is not possible to infer whether this is a shared characteristic of the family, or if higher EQs would be expected for other stem metatherians (Quiroga & Dozo, 1988, but see Weisbecker et al., 2021). The low EQ of *Sipalocyon* mainly derives from its relatively small cerebrum, a condition also observed in other fossil non-marsupial metatherians when compared to extant marsupials (Weisbecker et al., 2021). In the case of *Sipalocyon*, olfactory bulb volume is small in comparison to other metatherians, which contributes to an even lower EQ.

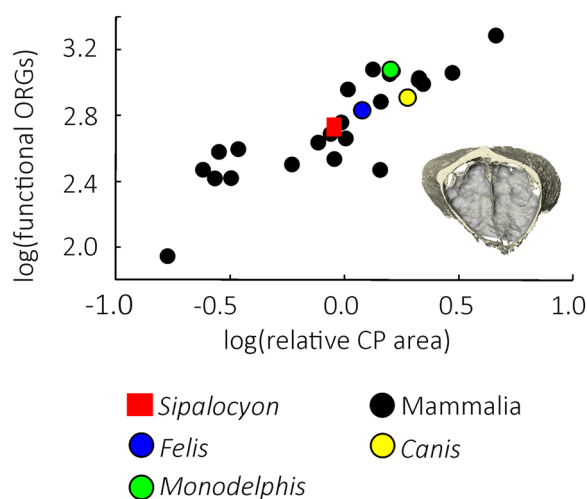


**Fig. 11** Log of the functional olfactory gene receptors (ORG) according to the log of the relative cribriform plate area modified from Bird et al. (2018). Marsupial and carnivoran mammals similar to *S. externus* are indicated in colors. Area of interest from the cribriform plate is illustrated with the same endocranial view that Fig. 4A

**Nasal structures and olfaction.** The anatomy of the nasal cavity of *S. externus* is close to that of marsupials, featuring one maxilloturbinal, one nasoturbinal, five endoturbinals, and two ectoturbinals (Fig. 4). The endo- and ectoturbinals are covered by olfactory epithelium in extant marsupials (Rowe et al., 2005), but the incomplete preservation of these turbinals in our material obviates comparative inferences.

In mammals, the cribriform plate is perforated by various divisions of the olfactory nerve (CNI; Figs. 4D and 9). The total perforated cribriform plate surface area is 83.20 mm<sup>2</sup>. With body mass estimation between 2.3 and 2.7 kg, the logarithmic relative cribriform plate surface area is -0.083–0.046. Using the regression of Bird et al. (2018), the number of functional olfactory receptor genes of *S. externus* is estimated to lie between 523 and 556. These values are much lower than the extant marsupial *Monodelphis domestica* (1188 receptor genes; Bird et al., 2018) but among carnivorous mammals, they approximate those of the extant felid *Felis silvestris catus* Schreber, 1775 (677; Bird et al., 2018; but see Additional file 1: Cribriform Plate Analysis) and the values predicted for the much larger saber-toothed felid *Smilodon fatalis* Leidy, 1868 (~600; Bird et al., 2018).

Lesser reliance on olfaction in *S. externus* is also reflected in its small olfactory bulbs, which represent only 5.8% of the encephalic cavity. This seems to be the general case for the genus *Sipalocyon* as the other two specimens studied have equally low olfactory bulb proportions (*S. gracilis*: 5.8%; *Sipalocyon* sp.: 5.7%). This percentage is smaller than that found not only in extant marsupials but also in the borhyaenid *Borhyaena tuberculata* (7.4%; calculated from Weisbecker et al., 2021) and the stem marsupials *Pucadelphys andinus* (11.7%; Macrini, 2007a) and *Andinodelphys cochabambensis* (12%; Muizon & Ladevèze, 2020). Small olfactory bulbs and lesser surface for olfactory nerve perforations on the cribriform plate are a strong indication that the olfactory system of *Sipalocyon* was not the primary sense used for hunting but was rather complementary to other sensorial capacities (vision, hearing, somesthesia).

**Orbit orientation and vision.** The orbits of *S. externus* and *S. gracilis* are highly convergent, a characteristic of predatory mammals that have large fields of stereoscopic vision—depth perception—for focusing on their prey (e.g., Cartmill, 1970; Gaillard et al., 2023; Heesy, 2004). Although hathliacynids and borhyaenids have different orbit orientations, in possible correlation with their respective locomotory behavior, the orbits of *Sipalocyon* are arranged like that of the borhyaenid *Arctodictis sinclairi* (Gaillard et al., 2023). Among sparassodonts, major differences in orbital angular relationships have been detected in the sabertooth *Thylacosmilus atrox*, but this

was a consequence of a major reorganization of its cranial anatomy to accommodate hyperdeveloped upper canines (Gaillard et al., 2023). In *Sipalocyon*, the convergence angle is similar to angles found in other carnivorous mammals that use sight to hunt prey. In fact, the majority of living hypercarnivorous felids (e.g., pumas, cheetahs) rely heavily on vision for predation (e.g., Kitchener, 1991; Van Valkenburgh et al., 2014), and we infer that this was also the case for *Sipalocyon*.

**Middle ear and audition.** In the absence of soft tissue preservation, features of middle ear elements such as the ectotympanic can help to estimate hearing capabilities in fossil taxa (e.g., Rosowski, 1992). The pars tensa of the tympanic membrane is reconstructed as a circular plane fitting the curvature of the crista tympani; the maximum diameter of the membrane is measured as the maximum distance of curvature (Additional file 1: Figure S14). In *S. externus*, the diameter of the reconstructed pars tensa is 4.7 mm and its area is 17.35 mm<sup>2</sup>. By applying the equation of Rosowski (1992), the estimated limits of optimum hearing frequencies of *S. externus* span the interval between 0.7 and 38.3 kHz. To test this estimation, we also calculated hearing frequency limits for *S. externus* according to Rosowski's (1992) equation using the size of the fenestra vestibuli, for which we obtained almost the same range of frequencies (0.5–37.9 kHz). These values, similar to the frequencies previously estimated for *S. gracilis* based on stapedial footplate dimensions (1.0–48.6 kHz; Gaillard et al., 2021), correspond to the hearing ranges of the extant dasyuromorph *Dasyurus hallucatus* (0.5–40 kHz; Aitkin et al., 1994; Vater et al., 2004).

**Inner ear and agility.** The radius of curvature of the semicircular canals is supposed to be a proxy for agility, agile mammals having significantly larger canals relative to body mass than slow-moving mammals (Spoor et al., 2007). Using the database generated by Spoor

et al. (2007), we added data from sparassodonts and other extant and extinct metatherians to assess agility in this group (Fig. 12; Additional file 1: Table S5). The graph shows that marsupials are often below the corresponding trend line for their category, while sparassodonts were close to slow and extra-slow mammals (Fig. 12). This is not congruent with their postcranial morphologies (Argot, 2003a, 2003b; Ercoli et al., 2012). The only sparassodont close to more agile species is *Thylacosmilus*. We consider that the trend found by Spoor et al. (2007) cannot be applied to our particular group, which possibly responds to phylogenetic constraints or sample bias against metatherians.

### Insights on the cranial venous drainage

**Diploic system.** One unexpected feature in *S. externus* MACN-Pv CH1911 revealed by the CT scans and the 3D reconstruction is the presence of a large accessory transverse diploic canal (atc) in the parietal diploic space. There are two large foramina through which the atc communicates with the primary transverse sinus (= foramina for parietal diploic vein sensu Muizon et al., 2018; Additional file 1: Figure S13). Similar foramina have also been reported in fossil and extant metatherians (*Allqokirus*, *Andinodelphys*, *Didelphis*, *Dromiciops*, *Thylacinus*, and *Dasyurus*; Muizon & Ladevèze, 2020). Additionally in *S. externus* a couple of tiny canaliculi (too small to be rendered in the 3D reconstruction) connect the atc to the reduced parietal diploic.

In *S. gracilis* AMNH VP-9254, the diploic system seems to be reduplicated. The left and right division of the atc pass rostrally into the parietal diploic to merge at the level of the confluence of sinuses to form a single, rostrocaudally oriented canal. This canal, called the accessory sagittal diploic canal (asc), travels through the diploic, parallel and dorsal to the superior sagittal sinus, to the level of the olfactory bulbs where it splits into four smaller canals and associated ramifications. There are many small connections between the atc and asc and the diploic space, although the latter is not very extensive. On the left side of the atc, another large diploic canal projects caudally, enters the interparietal diploic, and exits the cranium through emissary foramina (Fig. 13). The size of this canal is slightly smaller than the atc, which might indicate that part of the content of the atc drains into the interparietal diploic and the rest flows via the prootic sinus (see below). There are also several irregularly distributed small apertures at the base of the sagittal and nuchal crests (e.g., Fig. 13; Additional file 1: Figure S11L). These are interpreted as diploic and emissarial foramina (for discussion of similar networks in panperissodactyls see MacPhee et al., 2021).

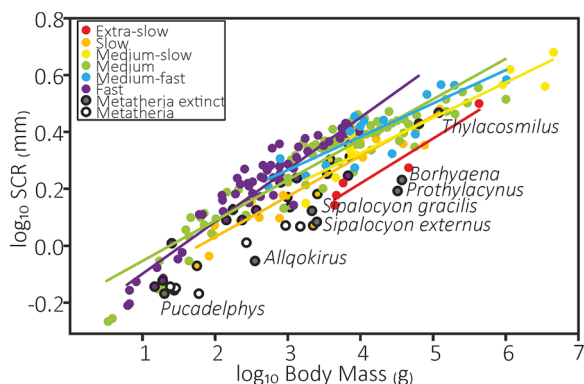


**Fig. 12** Log<sub>10</sub> of the average semicircular canal radius (see inner ear measurements and Additional file 1: Table S5) according to the Log<sub>10</sub> body mass, and agility. SCR semicircular canal radius Modified from Spoor et al. (2007).

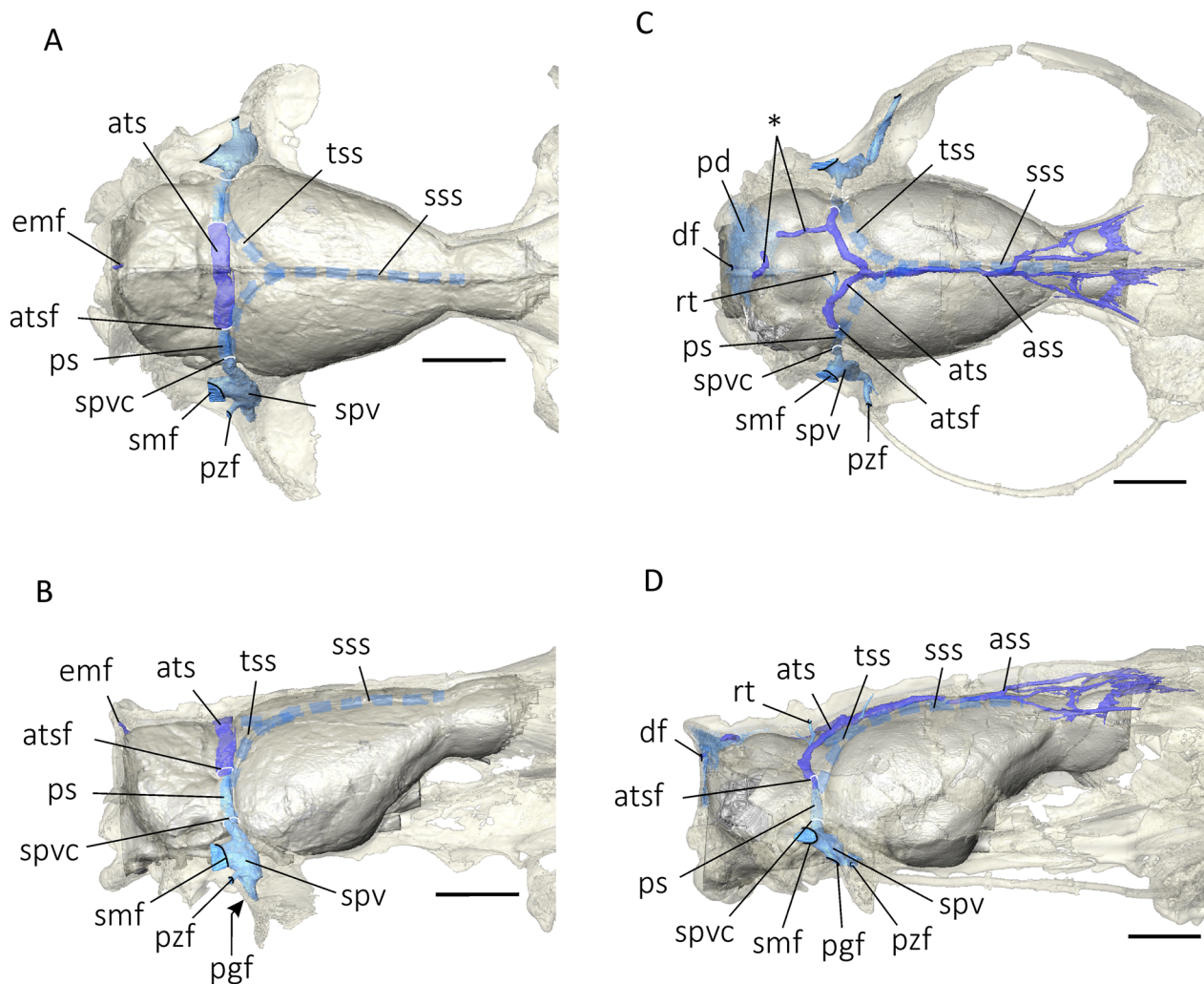


**Fig. 13** Digital reconstruction of the accessory transverse diploic sinus in **A–B** *S. externus* MACN-Pv CH1911 and **C–D** *S. gracilis* AMNH VP-9254 in dorsal (**A, C**) and lateral (**B, D**) views. Dark blue indicates the major dorsal diploic canals. In light blue are other features associated with the accessory transverse diploic canal (e.g., sphenoparietal emissary vein, interparietal diploic space). Discontinuous light blue lines represent the superior sagittal sinus and transverse sinus. Foramina in white are inside the encephalic cavity, whereas foramina in black are outside, on the cranial surface. Asterisk indicates major canals inside the interparietal diploic space for the interparietal diploic vein. Scale bars represent 1 cm. *ass* accessory superior sagittal diploic sinus, *ats* accessory transverse diploic sinus, *atsf* foramen for the accessory transverse diploic sinus, *df* diploic foramen, *emf* emissary foramen, *pd* parietal diploe, *pgf* postglenoid foramen, *ps* prootic sinus, *pzf* postzygomatic foramen, *rt* rami temporales, *smf* suprameatal foramen, *spv* sphenoparietal emissary vein, *spvc* canal for the sphenoparietal vein, *sss* superior sagittal sinus, *tss* transverse sinus

**Postglenoid venous system.** In *Sipalocyon*, the prootic sinus runs along a sulcus between the petrosal and squamosal (Fig. 13). The prootic sinus, now enlarged by the venous flow of the transverse sinus and the accessory transverse diploic sinus, leaves the encephalic cavity via the sphenoparietal emissary vein through the postglenoid foramen (postglenoid vein in Wible, 2003, 2022). Inside the squamosal there is a large canal that we interpret as the common trunk of the sphenoparietal emissary vein

and its branch, the suprameatal vein. The later exits the cranium at the suprameatal foramen (Wible, 2022). This network finally drains into the external jugular vein. Piercing the squamosal, the postzygomatic foramen also communicates with the postglenoid canal via a small conduit (Fig. 13, Additional file 1: Figure S11G).

The configuration of squamosal vasculature of *Sipalocyon* is typical of marsupials (e.g., Wible, 2003, 2022), apart from its larger size due to additional venous components related to the accessory transverse diploic sinus.

## Conclusion

The two sparassodonts described here represent the known mammalian carnivore fauna of the Early Miocene Colhuehuapian locality of Sacanana (Patagonia, Argentina): the small-bodied *Sipalocyon externus* and the larger *Borhyaena macrodonta*. The well-preserved cranium of *S. externus* MACN-Pv CH1911 allowed a complete  $\mu$ CT-assisted study of its anatomy. The incomplete specimen MACN-Pv CH40 is referred to the species *Borhyaena macrodonta*.

The cranial anatomy of *S. externus* is similar in various ways to that of other metatherians (e.g., five endoturbinals, large cerebellum). CT scanning permitted discovery of a number of other features: palatine canal for major palatine nerve and associated vasculature enclosed within hard palate (instead of having a major palatine foramen or fenestra); relatively small paraflocculi and olfactory bulbs compared to the volume of the braincase endocast; exposure of midbrain; presence of large accessory transverse diploic sinus inside the parietal diploe draining into postglenoid venous system; and well-pneumatized middle ear cavity. The majority of these are probably present in other sparassodont taxa that have yet to be studied tomographically.

The body size of *S. externus* is estimated at 2.3–2.7 kg, similar to previous estimations based on dental measurements (Prevosti et al., 2013; Zimicz, 2014). Thus, *S. externus* was a small predator, among the smallest species of thylacynids.

The encephalization quotient of *S. externus* is smaller than that of borhyanoid sparassodonts (*Borhyaena tuberculata*, *Thylacosmilus atrox*, although body mass of the two species is pending updating), it is larger than that of the fossil metatherian sister taxon of sparassodonts (*Pucadelphys andinus*), and fits within the range of EQs found in extant marsupials.

The small olfactory bulbs suggest that *S. externus* had lesser sense of smell than extant marsupials. The number of functional olfactory receptor genes, as estimated from the cribriform plate, also suggests that the capacity to interpret olfactory information at the receptor level was more limited than that of extant marsupials, perhaps close to that of domestic cats. The optimal hearing frequency limits of *S. externus* are estimated to lie between 0.5 and 55 kHz and resemble the frequency spectrum of extant marsupials. The orbital orientation of *S. externus* is typical of predatory mammals using wide-field stereoscopic vision, but not as extreme as extant felids. Altogether, *S. externus* does not show radical specialization in any of the three senses studied here (vision, audition, and smell), which argues for a complementary use of sensory capacities in its predatory behavior.

In conclusion, this study provides new information on the sparassodonts of the Early Miocene of Patagonia with a comprehensive study of the cranial anatomy and neuroanatomy of *Sipalocyon externus*. Such deep cranial investigations allow for many interpretations on the paleobiology of metatherian fossils and contribute to the understanding of the evolution of marsupials.

## Supplementary Information

The online version contains supplementary material available at <https://doi.org/10.1186/s13358-024-00312-x>.

**Additional file 1.** Supplemental figures and tables with additional information on the method.

## Acknowledgements

We would like to thank curators who permitted the study and scanning of specimens under their care A. Kramarz, S. Álvarez, L. Chornogubsky (former), and A. Martinelli (MACN), R. O'Leary and J. Galkin (AMNH), as well as S. F. Vizcaíno and S. Bargo (MLP) for granting access to sparassodonts specimen from their recent excavations housed at MPM; K. Le Verger (PIMUZ), A. Kramarz (MACN), and G. Rougier (UL) for their valuable comments during the development of the manuscript; Marta Bellato (AST-RX) for the CT scanning (Project ASTRX-2015-022); A. Boscaini for his help with tomographies; O. Maridet (JURASSICA) and S. Hernández del Pino (IANIGLA) for their assistance in the use of software for 3D reconstruction; and S. Laza (IANIGLA) for MEB photographs; M. R. Sánchez-Villagra and K. Le Verger for their meaningful revisions which greatly improved the manuscript.

## Author contributions

AMF designed the research. AMF, RDEM and SL conducted CT scans. CG and SDT segmented the tomographies. CG and AMF performed research, analyzed results, and wrote the paper with inputs from SDT, RDEM and SL.

## Funding

This study is a contribution to the project PICT 2019-2874, funded by the Agencia Nacional de Promoción Científica y Tecnológica (ANPCyT).

## Availability of data and materials

All data supporting the findings of this study are available within the paper and its additional file. CT scans and derivatives are available through the museum in which the specimens are deposited.

## Declarations

### Competing interests

The authors declare no competing interests.

### Author details

<sup>1</sup>Instituto Argentino de Nivología, Glaciología y Ciencias Ambientales (IANIGLA), CONICET-UNCUYO-Gob. Mza., Av. Ruiz Leal s/n Parque General San Martín, CP 5500 Mendoza, Argentina. <sup>2</sup>Centre de Recherche en Paléontologie, Paris (CR2P, UMR 7207), MNHN CNRS Sorbonne Université, Muséum national d'Histoire naturelle, 57 rue Cuvier CP 38, 75005 Paris, France. <sup>3</sup>Department of Mammalogy, Division of Vertebrate Zoology, American Museum of Natural History, 200 Central Park West, New York 10024-5102, USA.

Received: 8 November 2023 Accepted: 15 February 2024

Published online: 21 May 2024

## References

Abello, M. A. (2007). *Sistemática y bioestratigrafía de los Paucituberculata (Mammalia, Marsupialia) del Cenozoico de América del Sur*. [Doctoral

- dissertation, Universidad Nacional de La Plata]. Available at: <http://natura.fcnym.unlp.edu.ar/id/20120126000025>. Accessed 15 October 2021.
- Abràmoff, M. D., Magalhães, P. J., & Ram, S. J. (2004). Image processing with ImageJ. *Biophotonics International*, 11(7), 36–42.
- Aitkin, L. M. (1998). *Hearing—The Brain and Auditory Communication in Marsupials*. Springer-Verlag.
- Aitkin, L. M., Nelson, J. E., & Shepherd, R. K. (1994). Hearing, vocalization and the external ear of a marsupial, the Northern quoll, *Dasyurus hallucatus*. *The Journal of Comparative Neurology*, 349(3), 377–388. <https://doi.org/10.1002/cne.903490305>
- Allen, H. (1882). On a revision of the ethmoid bone in the Mammalia, with special reference to the description of this bone and the sense of smelling in the Cheiroptera. *Bulletin of the Museum of Comparative Zoology*, 10(3), 135–171.
- Archer, M. (1976). The basicranial region of marsupial carnivores (Marsupialia), interrelationships of carnivorous marsupials, and affinities of the insectivorous marsupial peramelids. *Zoological Journal of the Linnean Society*, 59(3), 217–322. <https://doi.org/10.1111/j.1096-3642.1976.tb01016.x>
- Argot, C. (2003a). Postcranial functional adaptations in the South American Miocene borhyaenoids (Mammalia, Metatheria): *Cladosictis*, *Pseudonotictis* and *Sipalocyon*. *Alcheringa an Australasian Journal of Palaeontology*, 27(4), 303–356. <https://doi.org/10.1080/03115510308619110>
- Argot, C. (2003b). Functional adaptations of the postcranial skeleton of two Miocene borhyaenoids (Mammalia, Metatheria), *Borhyaena* and *Prothylacinus*, from South America. *Palaeontology*, 46(6), 1213–1267. <https://doi.org/10.1046/j.0031-0239.2003.00339.x>
- Arnal, M., & Kramarz, A. G. (2011). First complete skull of an octodontoid (Rodentia, Caviomorpha) from the Early Miocene of South America and its bearing in the early evolution of Octodontoidea. *Geobios*, 44, 435–444. <https://doi.org/10.1016/j.geobios.2010.12.003>
- Babot, M. J., Powell, J. E., & de Muizon, C. (2002). *Callistoe vincei*, a new Proboscidea (Borhyaenoidea, Metatheria, Mammalia) from the Early Eocene of Argentina. *Geobios*, 35, 615–629. [https://doi.org/10.1016/S0016-6995\(02\)00073-6](https://doi.org/10.1016/S0016-6995(02)00073-6)
- Babot, M. J., Rougier, G. W., García-López, D. A., Bertelli, S. B., Herrera, C. M., Deraco, M. V., & Giannini, N. P. (2022). New mandibular remains of *Callistoe* (Metatheria, Sparassodonta) reveal unexpected anatomical, functional, and evolutionary aspects of this carnivorous genus. *Vertebrate Zoology*, 72, 469–485. <https://doi.org/10.3897/vz.72.e82709>
- Barreda, V., & Palazzesi, F. (2010). Vegetation during the Eocene-Miocene interval in central Patagonia: A context of mammal evolution. In R. H. Madden, A. A. Carlini, M. G. Vucetich, & R. F. Kay (Eds.), *The Paleontology of Gran Barranca: Evolution and Environmental Change through the Middle Cenozoic of Patagonia* (pp. 375–382). Cambridge University Press.
- Barreda, V., & Palazzesi, F. (2014). Response of plant diversity to Miocene forcing events: The case of Patagonia. In W. D. Stevens, O. M. Montiel, & P. H. Raven (Eds.), *Paleobotany and Biogeography: A Festschrift for Alan Graham in His 80th Year* (pp. 1–25). Annals of the Missouri Botanical Garden.
- Barrio, C., Carlini, A. A., & Goin, F. J. (1989). Litogénesis y antigüedad de la Formación Chichinales de Paso Córdoba (Río Negro, Argentina). 4º Congreso Argentino de Paleontología y Bioestratigrafía (Mendoza, 1986). *Actas*, 4, 149–156.
- Beck, R. M. D., Voss, R. S., & Jansa, S. A. (2022). Craniodental morphology and phylogeny of marsupials. *Bulletin of the American Museum of Natural History*, 457, 1–350. <https://doi.org/10.1206/0003-0090.457.1.1>
- Bellosi, E. S., Genise, J. F., Zucol, A. F., Bond, M., Kramarz, M., Sánchez, M. V., & Krause, J. M. (2021). Diverse evidence for grasslands since the Eocene in Patagonia. *Journal of South American Earth Sciences*, 108, 103357. <https://doi.org/10.1016/J.JSAMES.2021.103357>
- Bellosi, E. S., & Gonzalez, M. G. (2010). Paleosols of the middle Cenozoic Sarmiento Formation, central Patagonia. In R. H. Madden, A. A. Carlini, M. G. Vucetich, & R. F. Kay (Eds.), *The Paleontology of Gran Barranca: Evolution and Environmental Change through the Middle Cenozoic of Patagonia*. Cambridge University Press.
- Bertrand, O. C., Farah, A.-M., Lang, M. M., & Silcox, M. T. (2019). New virtual endocasts of Eocene Ischryomyidae and their relevance in evaluating neurological changes occurring through time in Rodentia. *Journal of Mammalian Evolution*, 26(3), 345–371. <https://doi.org/10.1007/s10914-017-9425-6>
- Bertrand, O. C., Shelley, S. L., Wible, J. R., Williamson, T. E., Holbrook, L. T., Chester, S. G. B., Butler, I. B., & Brusatte, S. L. (2020). Virtual endocranial and inner ear endocasts of the Paleocene 'condylarth' *Chriacus*: New insight into the neurosensory system and evolution of early placental mammals. *Journal of Anatomy*, 236(1), 21–49. <https://doi.org/10.1111/joa.13084>
- Billet, G., Germain, D., Ruf, I., de Muizon, C., & Hautier, L. (2013). The inner ear of *Megatherium* and the evolution of the vestibular system in sloths. *Journal of Anatomy*, 223, 557–567. <https://doi.org/10.1111/joa.12114>
- Bird, D. J., Amirkhanian, A., Pang, B., & Van Valkenburgh, B. (2014). Quantifying the cribriform plate: Influence of allometry, function, and phylogeny in Carnivora. *The Anatomical Record*, 297(11), 2080–2092. <https://doi.org/10.1002/ar.23032>
- Bird, D. J., Murphy, W. J., Fox-Rosales, L., Hamid, I., Eagle, R. A., & Van Valkenburgh, B. (2018). Olfaction written in bone: Cribriform plate size parallels olfactory receptor gene repertoires in Mammalia. *Proceedings of the Royal Society b: Biological Sciences*, 285(1874), 20180100. <https://doi.org/10.1098/rspb.2018.0100>
- Blanks, R. H. I., Curthoys, I. S., & Markham, C. H. (1975). Planar relationships of the semicircular canals in man. *Acta Oto-Laryngologica*, 80, 185–196.
- Bown, T. M., & Fleagle, G. F. (1993). Systematics, Biostratigraphy, and dental evolution of the Palaeothentidae, Later Oligocene to Early-Middle Miocene (Deseadan-Santacrucian) Caenolestoid marsupials of South America. *Journal of Paleontology*, 67, 1–76. <https://doi.org/10.1017/S0022336000062107>
- Bucher, J., Pérez, M. E., González Ruiz, L. R., D'Elía, L., & Bिल्mes, A. (2021). New middle Miocene (Langhian—Serravallian) vertebrate localities in northwestern Patagonia, Argentina: A contribution to high latitude South American Land Mammal Ages sequence. *Journal of South American Earth Sciences*, 107, 1–15. <https://doi.org/10.1016/j.jsames.2020.103024>
- Cartmill, M. (1970). The orbits of arboreal mammals: a reassessment of the arboreal theory of primate evolution. [Doctoral dissertation, University of Chicago].
- Croft, D. A., Engelman, R. K., Dolgushina, T., & Wesley, G. (2017). Diversity and disparity of sparassodonts (Metatheria) reveal non-analogue nature of ancient South American mammalian carnivore guilds. *Proceedings of the Royal Society B*, 285, 20172012. <https://doi.org/10.1098/rspb.2017.2012>
- David, R., Droulez, J., Allain, R., Berthoz, A., Janvier, P., & Bennequin, D. (2010). Motion from the past. A new method to infer vestibular capacities of extinct species. *Compte Rendu Palevol*, 9, 397–410. <https://doi.org/10.1016/j.crpv.2010.07.012>
- de Muizon, C. (1999). Marsupial skulls from the Deseadan (Late Oligocene) of Bolivia and phylogenetic analysis of the Borhyaenoidea (Marsupialia, Mammalia). *Geobios*, 32(3), 483–509. [https://doi.org/10.1016/S0016-6995\(99\)80022-9](https://doi.org/10.1016/S0016-6995(99)80022-9)
- de Muizon, C., Cifelli, R. L., & Paz, R. C. (1997). The origin of the dog-like borhyaenoid marsupials of South America. *Nature*, 389, 486–489. <https://doi.org/10.1038/39029>
- de Muizon, C., & Ladevèze, S. (2020). Cranial anatomy of *Andinodelphys cochabambensis*, a stem metatherian from the early Palaeocene of Bolivia. *Geodiversitas*, 42(30), 597–739. <https://doi.org/10.5252/geodiversitas2020v42a30>
- de Muizon, C., Ladevèze, S., Selva, C., Vignaud, R., & Goussard, F. (2018). *Allqokirus australis* (Sparassodonta, Metatheria) from the early Palaeocene of Tiupampa (Bolivia) and the rise of the metatherian carnivorous radiation in South America. *Geodiversitas*, 40(3), 363–459. <https://doi.org/10.5252/geodiversitas2018v40a16>
- De Vleeschouwer, D., Vahlenkamp, M., Crucifix, M., & Pálke, H. (2017). Alternating Southern and Northern Hemisphere climate response to astronomical forcing during the past 35 m.y. *Geology*, 45(4), 375–378. <https://doi.org/10.1130/G38663.1>
- Dozo, M. T. (1989). Estudios paleoneurológicos en Didelphidae extinguidos (Mammalia, Marsupialia) de la Formación Chapadmalal (Plioceno tardío), Provincia de Buenos Aires, Argentina. *Ameghiniana*, 26(1–2), 43–54.
- Dozo, M. T. (1994). Estudios paleoneurológicos en marsupiales “carnívoros” extinguidos de América del Sur: Neuromorfología y encefalización. *Mastozoología Neotropical*, 1, 5–16.
- Dunn, R. E., Madden, R. H., John, M. J., Schmitz, M. D., Strömberg, A. E., Carlini, A. A., Ré, G. H., & Crowley, J. (2013). A new chronology for middle Eocene–early Miocene South American Land Mammal Ages. *GSA Bulletin*, 125(3/4), 539–555. <https://doi.org/10.1130/B30660.1>
- Echarri, S., Ulloa-Guaiquin, K. S., Aguirreayala, G., & Forasiépi, A. M. (2021). *Cladosictis patagonica* (Metatheria, Sparassodonta) from the Collón Cura

- Formation (Middle Miocene), Río Negro, Argentina. *Ameghiniana*, 58(6), 485–491. <https://doi.org/10.5710/AMGH.06.08.2021.3439>
- Eisenberg, J. F. (1981). *The mammalian radiation. An Analysis of trends in evolution, adaptation, and behavior*. The University of Chicago Press.
- Ekdale, E. G. (2010). Ontogenetic variation in the bony labyrinth of *Monodelphis domestica* (Mammalia: Marsupialia) following ossification of the inner ear cavities. *The Anatomical Record Advances in Integrative Anatomy and Evolutionary Biology*, 293, 1896–1912. <https://doi.org/10.1002/ar.21234>
- Ekdale, E. G. (2013). Comparative anatomy of the bony labyrinth (inner ear) of placental Mammals. *PLoS ONE*, 8, e66624. <https://doi.org/10.1371/journal.pone.0066624>
- Ekdale, E. G. (2015). Form and function of the mammalian inner ear. *Journal of Anatomy*, 228(2), 324–337. <https://doi.org/10.1111/joa.12308>
- Ercoli, M. D., & Prevosti, F. J. (2011). Estimación de Masa de las Especies de Sparassodonta (Mammalia, Metatheria) de Edad Santacrucense (Mioceno Temprano) a Partir del Tamaño del Centroide de los Elementos Apendiculares: Inferencias Paleocológicas. *Ameghiniana*, 48(4), 426–479. [https://doi.org/10.5710/AMGH.v48i4\(347\)](https://doi.org/10.5710/AMGH.v48i4(347))
- Ercoli, M. D., Prevosti, F. J., & Álvarez, A. (2012). Form and function within a phylogenetic framework: Locomotory habits of extant predators and some Miocene Sparassodonta (Metatheria). *Zoological Journal of the Linnean Society*, 165(1), 224–251. <https://doi.org/10.1111/j.1096-3642.2011.00793.x>
- Evans, H. E., & de Lahunta, A. (2013). *Miller's Anatomy of the dog* (4th ed.). Elsevier.
- Fedorov, A., Beichel, R., Kalpathy-Cramer, J., Finet, J., Fillion-Robin, J.-C., Pujol, S., Bauer, C., Jennings, D., Fennessy, F., Sonka, M., Buatti, J., Aylward, S., Miller, J. V., Pieper, S., & Kikinis, R. (2012). 3D Slicer as an image computing platform for the Quantitative Imaging Network. *Magnetic Resonance Imaging*, 30(9), 1323–1341. <https://doi.org/10.1016/j.mri.2012.05.001>
- Fleagle, J. G., & Bown, T. M. (1983). New primate fossils from Late Oligocene (Colhuehuapian) localities of Chubut province, Argentina. *Folia Primatologica*, 41, 240–266. <https://doi.org/10.1159/000156135>
- Flynn, J. J., Charrier, R., Croft, D. A., Gans, P. B., Herriott, T. M., Wertheim, J. A., & Wyss, A. R. (2008). Chronologic implications of new Miocene mammals from the Cura-Mallín and Trapa Trapa formations, Laguna del Laja area, south central Chile. *Journal of South American Earth Sciences*, 26(4), 412–423. <https://doi.org/10.1016/j.jsames.2008.05.006>
- Forasiepi, A. M. (2009). Osteology of *Arctodictis sinclairi* (Mammalia, Metatheria, Sparassodonta) and phylogeny of Cenozoic metatherian carnivores from South America. *Monografías Del Museo Argentino De Ciencias Naturales*, 6, 1–174.
- Forasiepi, A. M., Babet, M. J., & Zimicz, A. N. (2015). *Australoayaena antiqua* (Mammalia, Metatheria, Sparassodonta), a large predator from the late Oligocene of Patagonia. *Journal of Systematic Palaeontology*, 13, 505–523. <https://doi.org/10.1080/14772019.2014.926403>
- Forasiepi, A. M., MacPhee, R. D. E., & Hernández del Pino, S. (2019). Caudal cranium of *Thylacosmilus atrox* (Mammalia, Metatheria, Sparassodonta), a South American predaceous sabertooth. *Bulletin of the American Museum of Natural History*, 433, 1–64. <https://doi.org/10.1206/0003-0090.433.1.1>
- Forasiepi, A. M., & Sánchez-Villagra, M. R. (2014). Heterochrony, dental ontogenetic diversity, and the circumvention of constraints in marsupial mammals and extinct relatives. *Paleobiology*, 40, 222–237. <https://doi.org/10.1666/13034>
- Forasiepi, A. M., Sánchez-Villagra, M. R., Goin, F. J., Masanaru, T., Nobuo, S., & Kay, R. (2006). A new species of Hathliacynidae (Metatheria, Sparassodonta) from the middle Miocene of Quebrada Honda, Bolivia. *Journal of Vertebrate Paleontology*, 26(3), 670–684. [https://doi.org/10.1671/0272-4634\(2006\)26\[670:ANSOHM\]2.0.CO;2](https://doi.org/10.1671/0272-4634(2006)26[670:ANSOHM]2.0.CO;2)
- Gaillard, C., MacPhee, R. D. E., & Forasiepi, A. M. (2021). The stapes of stem and extinct Marsupialia: Implications for the ancestral condition. *Journal of Vertebrate Paleontology*, 41(2), e1924761. <https://doi.org/10.1080/02724634.2021.1924761>
- Gaillard, C., MacPhee, R. D. E., & Forasiepi, A. M. (2023). Seeing through the eyes of the sabertooth *Thylacosmilus atrox* (Metatheria, Sparassodonta). *Communications Biology*, 6, 257. <https://doi.org/10.1038/s42003-023-04624-5>
- Garrido, A., Kramarz, A., Forasiepi, A., & Bond, M. (2012). Estratigrafía, mamíferos fósiles y edad de las secuencias volcánico-sedimentarias cenozoicas de la Sierra de Huantraico-Sierra Negra y Cerro Villegas (provincia del Neuquén, Argentina). *Andean Geology*, 39, 482–510. <https://doi.org/10.5027/andgeoV39n3-a07>
- Gaudin, T. J., Wible, J. R., Hopson, J. A., & Turnbull, W. D. (1996). Reexamination of the morphological evidence for the cohort epithelia (Mammalia, Eutheria). *Journal of Mammalian Evolution*, 3(1), 31–79. <https://doi.org/10.1007/BF01454253>
- Goin, F. J., Abello, A., Bellosi, E., Kay, R., & Madden, R. (2007). Los Metatheria sudamericanos de comienzos del Neógeno (Mioceno Temprano, Edad mamífero Colhuehuapense). Parte I: Introducción. *Didelphimorphia y Sparassodonta. Ameghiniana*, 44(1), 29–74.
- Goin, F. J., Woodburne, M. O., Zimicz, A. N., Martin, G. M., & Chornogubsky, L. (2016). *A brief history of South American metatherians: Evolutionary contexts and intercontinental dispersals*. Springer.
- Gordon, C. L. (2003). A first look at estimating body size in dentally conservative marsupials. *Journal of Mammal Evolution*, 10, 1–21. <https://doi.org/10.1023/A:1025545023221>
- Haight, J. R., & Nelson, J. E. (1987). A brain that doesn't fit its skull: a comparative study of the brain and endocranium of the koala, *Phascolarctos cinereus* (Marsupialia: Phascolarctidae). In M. Archer (Ed.), *Possums and opossums: studies in evolution* (pp. 331–352). Surrey Beatty and Sons Pty Limited.
- Hartwick, W. C. (1995). Effect of life history on the squirrel monkey (Platyrrhini, *Saimiri*) cranium. *American Journal of Physical Anthropology*, 97, 435–449. <https://doi.org/10.1002/ajpa.1330970409>
- Heesy, C. P. (2004). On the relationship between orbit orientation and binocular visual field overlap in mammals. *Anatomical Records A*, 281A, 1104–1110. <https://doi.org/10.1002/ar.a.20116>
- Heesy, C. P. (2005). Function of the mammalian postorbital bar. *Journal of Morphology*, 264, 363–380. <https://doi.org/10.1002/jmor.10334>
- Heffner, R. S. (2004). Primate hearing from a mammalian perspective. *The Anatomical Record Part A*, 281A, 1111–1122. <https://doi.org/10.1002/ar.a.20117>
- Hershkovitz, P. (1974). A new genus of Late Oligocene monkey (Cebidae, Platyrrhini) with notes on postorbital closure and platyrrhine evolution. *Folia Primatologica*, 21(1), 1–35.
- Hiiemae, K., & Jenkins, F. A. (1969). The anatomy and internal architecture of the muscles of mastication in *Didelphis marsupialis*. *Postilla*, 140, 1–49.
- Horovitz, I., Ladevèze, S., Argot, C., Macrini, T. E., Martin, T., Hooker, J. J., Kurz, C., de Muizon, C., & Sánchez-Villagra, M. R. (2008). The anatomy of Herpetotherium cf fugax Cope, a metatherian from the Oligocene of North America. *Palaeontographica Abteilung*, 284(4–6), 109–141. <https://doi.org/10.1127/pala/284/2008/109>
- Hurum, J. H. (1998). The inner ear of two Late Cretaceous multituberculate mammals, and its implications for multituberculate hearing. *Journal of Mammalian Evolution*, 5(1), 65–93. <https://doi.org/10.1023/A:1020571003901>
- Huxley, T. H. (1880). On the application of the laws of evolution to the arrangement of the Vertebrata, and more particularly of the Mammalia. *Proceedings of the Scientific Meetings of the Zoological Society of London*, 43, 649–662.
- Jerison, H. J. (1973). *Evolution of the brain and intelligence*. Academic Press.
- Jerison, H. J. (1991). Fossil brains and the evolution of the neocortex. In B. L. Finlay, G. Innocenti, & H. Scheich (Eds.), *The neocortex* (pp. 5–19). Springer Boston.
- Kaas, J. H. (2017). *Evolution of nervous systems*. Elsevier Academic Press.
- Kay, R. F. (2010). A new primate from the early Miocene of Gran Barranca, Chubut Province, Argentina: Paleogeological implications. In R. H. Madden, A. A. Carlini, M. G. Vucetich, & R. F. Kay (Eds.), *The Paleontology of Gran Barranca: Evolution and Environmental Change through the Middle Cenozoic of Patagonia* (pp. 220–239). Cambridge University Press.
- Kay, R. F., Campbell, V. M., Rossie, J. B., Colbert, M. W., & Rowe, T. B. (2004). Olfactory fossa of *Tremacebus harringtoni* (Platyrrhini, Early Miocene, Sacanana, Argentina): Implications for activity pattern. *The Anatomical Record*, 281A, 1157–1172. <https://doi.org/10.1002/ar.a.20121>
- Kay, R. F., Madden, R. H., Vucetich, G. M., Carlini, A. A., Mazzoni, M. M., Re, G. H., Heizler, M., & Sandeman, H. (1999). Revised geochronology of the Casamayoran South American Land Mammal Age: Climatic and biotic implications. *Proceedings of the National Academy of Sciences*, 96, 13235–13240. <https://doi.org/10.1073/pnas.96.23.13235>

- Kitchener, A. C., Van Valkenburgh, B., & Yamaguchi, N. (2010). Felid form and function. In D. W. Macdonald & A. J. Loveridge (Eds.), *Biology and conservation of wild felids* (pp. 83–106). Oxford University Press.
- Koyabu, D., Maier, W., & Sánchez-Villagra, M. R. (2012). Paleontological and developmental evidence resolve the homology and dual embryonic origin of a mammalian skull bone, the interparietals. *Proceedings of the National Academy of Sciences*, 109(35), 14075–14080. <https://doi.org/10.1073/pnas.1208693109>
- Kramarz, A., Garrido, A. C., Forasiepi, A. M., Bond, M., & Tambussi, C. (2005). Estratigrafía y vertebrados (Aves y Mammalia) de la Formación Cerro Bandera, Mioceno Temprano de la Provincia del Neuquén. *Argentina. Revista Geológica De Chile*, 32(2), 73–291. <https://doi.org/10.4067/S0716-02082005000200006>
- Kupczyńska, M., Czubaj, N., Barszcz, K., Sokołowski, W., Czopowicz, M., Puryzyc, H., Dzierżęcka, M., Kinda, W., & Kiełbowicz, Z. (2017). Prevalence of dorsal notch and variation in the foramen magnum shape in dogs of different breeds and morphotypes. *Biologia*, 72(2), 230–237. <https://doi.org/10.1515/biolog-2017-0018>
- Le Verger, K., González Ruiz, L., & Billet, G. (2021). Comparative anatomy and phylogenetic contribution of intracranial osseous canals and cavities in armadillos and glyptodonts (Xenarthra, Cingulata). *Journal of Anatomy*, 239(6), 1473–1502. <https://doi.org/10.1111/joa.13512>
- Luo, Z., Crompton, A. W., & Lucas, S. G. (1995). Evolutionary origins of the mammalian promontorium and cochlea. *Journal of Vertebrate Paleontology*, 15(1), 113–121.
- MacPhee, R. D. E. (1981). Auditory regions of primates and eutherian insectivores. Morphology, ontogeny, and character analysis. *Contribution to Primatology*, 18, 1–282.
- MacPhee, R. D. E., & Forasiepi, A. M. (2022). Re-evaluating cranial pathways of the internal carotid artery in Notoungulata (Mammalia, Panperissodactyla). *Ameghiniana*, 59(2), 141–161. <https://doi.org/10.5710/AMGH.06.12.2021.3465>
- MacPhee, R. D. E., Gaillard, C., Forasiepi, A. M., & Sulser, R. B. (2023). Transverse canal foramen and pericarotid venous network in metatheria and other mammals. *Bulletin of the American Museum of Natural History*, 462, 1–122. <https://doi.org/10.1206/0003-0090.462.1.1>
- MacPhee, R. D. E., Hernández Del Pino, S., Kramarz, A., Forasiepi, A. M., Bond, M., & Sulser, R. B. (2021). Cranial morphology and phylogenetic relationships of *Trigonostylops wortmani*, an Eocene South American native ungulate. *Bulletin of the American Museum of Natural History*, 449, 1–183. <https://doi.org/10.1206/0003-0090.449.1.1>
- Macrini, T. E. (2006). *The evolution of endocranial space in mammals and non-mammalian cynodonts*. [Doctoral dissertation, The University of Texas, Austin]. Texas Digital Library. <https://tdl-ir.tdl.org/items/2dc493fe-2e63-48b6-a297-07991ec8e1e2>.
- Macrini, T. E. (2012). Comparative morphology of the internal nasal skeleton of adult marsupials based on X-ray computed tomography. *Bulletin of the American Museum of Natural History*, 365, 1–91. <https://doi.org/10.1206/365.1>
- Macrini, T. E., Leary, M., & Weisbecker, V. (2022). Evolution of the brain and sensory structures in metatherians. In M. T. Dozo, A. Paulina-Carabajal, T. E. Macrini, & S. Walsh (Eds.), *Paleoneurology of amniotes*. Springer Nature Switzerland. [https://doi.org/10.1007/978-3-031-13983-3\\_11](https://doi.org/10.1007/978-3-031-13983-3_11)
- Macrini, T. E., Muizon, C., de Cifelli, R. L., & Rowe, T. (2007a). Digital cranial endocast of *Pucadelphys andinus*, a Paleocene metatherian. *Journal of Vertebrate Paleontology*, 27(1), 99–107. [https://doi.org/10.1671/0272-4634\(2007\)27\[99:DCEOPA\]2.0.CO;2](https://doi.org/10.1671/0272-4634(2007)27[99:DCEOPA]2.0.CO;2)
- Macrini, T. E., Rowe, T., & Archer, M. (2007b). Cranial endocasts from a growth series of *Monodelphis domestica* (Didelphidae, Marsupialia): A study of individual and ontogenetic variation. *Journal of Morphology*, 268(10), 844–865. <https://doi.org/10.1002/jmor.10556>
- Madden, R. H., Carlini, A. A., Vucetich, M. G., & Kay, R. F. (2010). *The Paleontology of Gran Barranca: Evolution and Environmental Change through the Middle Cenozoic of Patagonia*. Cambridge University Press.
- Maier, W. (1983). Morphology of the interorbital region of *Saimiri sciureus*. *Folia Primatologica*, 41, 277–303. <https://doi.org/10.1159/000156137>
- Marshall, L. G. (1977). A new species of Lycopsis (Borhyaenidae: Marsupialia) from the La Venta fauna (Late Miocene) of Colombia, South America. *Journal of Paleontology*, 51(3), 633–642.
- Marshall, L. G. (1978). Evolution of the Borhyaenidae, extinct South American predaceous marsupials. *University of California Publications in Geological Sciences*, 117, 1–89.
- Marshall, L. G. (1979). Review of the Prothylacyninae, an extinct subfamily of South American “dog-like” marsupials. *Fieldiana Geology*, 3, 1–50.
- Marshall, L. G. (1981). Review of the Hathlyacyninae, an extinct subfamily of South American “dog-like” marsupials. *Fieldiana Geology*, 7, 1–120.
- Myers, T. J. (2001). Prediction of marsupial body mass. *Australian Journal of Zoology*, 49, 99–118. <https://doi.org/10.1071/ZO01009>
- O’Leary, M. A., Bloch, J. I., Flynn, J. J., Gaudin, T. J., Giallombardo, A., Giannini, N. P., Goldberg, S. L., Kraatz, B. P., Luo, Z.-X., Meng, J., Ni, X., Novacek, M. J., Perini, F. A., Randall, Z. S., Rougier, G. W., Sargis, E. J., Silcox, M. T., Simmons, N. B., Spaulding, M., Velazco, P. M., ... Cirranello, A. L. (2013). The placental mammal ancestor and the post-K-Pg radiation of placentals. *Science*, 339(6120), 662–667. <https://doi.org/10.1126/science.1229237>
- Pavan, S. E., & Voss, R. S. (2016). A revised subgeneric classification of short-tailed opossums (Didelphidae: Monodelphis). *American Museum Novitates*, 3868, 1–44. <https://doi.org/10.1206/3868.1>
- Prevosti, F. J., & Forasiepi, A. M. (2018). Evolution of South American mammalian predators during the Cenozoic: Paleobiogeographic and paleoenvironmental contingencies. *Springer International Publishing*. <https://doi.org/10.1007/978-3-319-03701-1>
- Prevosti, F. J., Forasiepi, A. M., & Zimic, N. (2013). The evolution of the Cenozoic terrestrial mammalian predator guild in South America: Competition or replacement? *Journal of Mammalian Evolution*, 20, 3–21. <https://doi.org/10.1007/s10914-011-9175-9>
- Quiroga, J. C., & Dozo, M. T. (1988). The brain of *Thylacosmilus atrox*. Extinct South American saber-tooth carnivore marsupial. *Journal Für Hirnforschung*, 29(5), 573–586.
- Riggs, E. S. (1933). Preliminary description of a new marsupial sabertooth from the Pliocene of Argentina. *Geological Series of Field Museum of Natural History*, 6, 61–66.
- Riggs, E. S. (1934). A new marsupial saber-tooth from the Pliocene of Argentina and its relationships to other South American predaceous marsupials. *Transactions of the American Philosophical Society, New Series*, 24(1), 1–32.
- Rosenberger, A. L. (2019). *Dolichocebus gaimanensis* is not a stem platyrrhine. *Folia Primatologica*, 90(6), 494–506. <https://doi.org/10.1159/000500008>
- Rosowski, J. J. (1992). Hearing in transitional mammals: Predictions from the middle-ear anatomy and hearing capabilities of extant mammals. In D. B. Webster, A. N. Popper, & R. R. Kay (Eds.), *The evolutionary biology of hearing* (pp. 615–631). Springer-Verlag.
- Rossie, J. B. (2006). Ontogeny and homology of the paranasal sinuses in Platyrrhini (Mammalia: Primates). *Journal of Morphology*, 267, 1–40. <https://doi.org/10.1002/jmor.10263>
- Rowe, T. B., Eiting, T. P., Macrini, T. E., & Ketcham, R. A. (2005). Organization of the olfactory and respiratory skeleton in the nose of the gray short-tailed opossum *Monodelphis domestica*. *Journal of Mammalian Evolution*, 12(3/4), 303–336. <https://doi.org/10.1007/s10914-005-5731-5>
- Ruf, I., Luo, Z., Wible, J. R., & Martin, T. (2009). Petrosal anatomy and inner ear structures of the Late Jurassic *Henkelotherium* (Mammalia, Cladotheria, Dryolestidae): Insight into the early evolution of the ear region in cladotherian mammals. *Journal of Anatomy*, 214, 679–693. <https://doi.org/10.1111/j.1469-7580.2009.01059.x>
- Rusconi, C. (1933). Nuevos restos de monos fósiles del Terciario antiguo de Patagonia. *Anales De La Sociedad Científica Argentina*, 116, 286–289.
- Rusconi, C. (1935a). Las especies de primates del oligoceno de Patagonia (gen. Homunculus). *Ameghiniana*, 1(2), 39–68.
- Rusconi, C. (1935b). Las especies de primates del oligoceno de Patagonia (gen. Homunculus) (continuación). *Ameghiniana*, 1(3), 71–100.
- Rusconi, C. (1935c). Las especies de primates del oligoceno de Patagonia (gen. Homunculus) (conclusión). *Ameghiniana*, 1(4), 103–125.
- Sánchez-Villagra, M. R., Ladevèze, S., Horovitz, I., Argot, C., Hooker, J. J., Macrini, T. E., Martin, T., Moore-Fay, S., de Muizon, C., Schmelzle, T., & Asher, R. J. (2007). Exceptionally preserved North American Paleogene metatherians: Adaptations and discovery of a major gap in the opossum fossil record. *Biology Letters*, 3, 318–322. <https://doi.org/10.1098/rsbl.2007.0090>
- Sánchez-Villagra, M. R., & Schmelzle, T. (2007). Anatomy and development of the bony inner ear in the woolly opossum, *Caluromys philander* (Didelphimorphia, Marsupialia). *Mastozoología Neotropical*, 14(1), 53–60.

- Silcox, M. T., Benham, A. E., & Bloch, J. I. (2010). Endocasts of *Microsypops* (Microsypopidae, Primates) and the evolution of the brain in primitive primates. *Journal of Human Evolution*, 58(6), 505–521. <https://doi.org/10.1016/j.jhevol.2010.03.008>
- Silcox, M. T., Dalmyn, C. K., & Bloch, J. I. (2009). Virtual endocast of *Ignacius graybullianus* (Paromomyidae, Primates) and brain evolution in early primates. *Proceedings of the National Academy of Sciences*, 106(27), 10987–10992. <https://doi.org/10.1073/pnas.0812140106>
- Simpson, G. G. (1940). Review of the mammal-bearing Tertiary of South America. *Proceedings of the American Philosophical Society*, 83(5), 649–709.
- Simpson, G. G. (1980). *Splendid Isolation. The Curious History of South American Mammals* (p. 266). Yale University Press.
- Sinclair, W. J. (1906). Mammalia of the Santa Cruz beds: Marsupialia. *Reports of the Princeton University Expeditions to Patagonia*, 4(3), 333–460.
- Sinclair, W. J. (1930). New carnivorous Marsupialia from the Deseado Formation of Patagonia. *Field Museum of Natural History, Geological Memories*, 1, 35–39.
- Smaers, J. B., Rothman, R. S., Hudson, D. R., Balanoff, A. M., Beatty, B., Dechmann, D. K. N., de Vries, D., Dunn, J. C., Fleagle, J. G., Gilbert, C. C., Goswami, A., Iwaniuk, A. N., Jungers, W. L., Kerney, M., Ksepka, D. T., Manger, P. R., Mongle, C. S., Rohlf, F. J., Smith, N. A., ... Safi, K. (2021). The evolution of mammalian brain size. *Science Advances*, 7, eabe2101. <https://doi.org/10.1126/sciadv.abe2101>
- Spoor, F. (2003). The semicircular canal system and locomotor behaviour, with special reference to hominin evolution. *Courier-Forschungsinstitut Senckenberg*, 243, 93–104.
- Spoor, F., Garland, T., Krovitz, G., Ryan, T. M., Silcox, M. T., & Walker, A. (2007). The primate semicircular canal system and locomotion. *Proceedings of the National Academy of Sciences*, 104(26), 10808–10812. <https://doi.org/10.1073/pnas.0704250104>
- Súarez, C., Forasiepi, A. M., Babot, M. J., Shinmura, T., Luque, J., Vanegas, R. D., Cadena, E. A., & Goin, F. (2023). A sabre-tooth predator from the Neotropics: cranial morphology of *Anachlysis gracilis* Goin, 1997 (Metatheria, Thylacosmilidae), based on new specimens from La Venta (Middle Miocene, Colombia). In Carrillo (Ed.), *Neotropical palaeontology: the Miocene La Venta biome. Geodiversitas*, 45(18), 497–572. <https://doi.org/10.5252/geodiversitas2023v45a18>
- Toeplitz, C. (1920). Bau und Entwicklung des Knorpelschädels von *Didelphis marsupialis*. *Zoologica*, 27(70), 1–83.
- Turnbull, W. D. (1970). Mammalian masticatory apparatus. *Fieldian. Geology*, 18(2), 149–356.
- Van Valkenburgh, B., Pang, B., Bird, D., Curtis, A., Yee, C., Wysocki, C., & Craven, B. A. (2014). Respiratory and olfactory turbinates in feliform and caniform carnivores: The influence of snout length. *The Anatomical Record*, 297, 2065–2079. <https://doi.org/10.1002/ar.23026>
- Vater, M., & Kössl, M. (2011). Comparative aspects of cochlear functional organization in mammals. *Hearing Research*, 273, 89–99. <https://doi.org/10.1016/j.heares.2010.05.018>
- Vater, M., Meng, J., & Fox, R. C. (2004). Hearing organ evolution and specialization: Early and later mammals. In G. A. Manley, R. R. Fay, & A. N. Popper (Eds.), *Evolution of the vertebrate auditory system* (pp. 256–288). Springer.
- Vizcaíno, S. F., Bargo, M. S., Kay, R. F., Fariña, R. A., Di Giacomo, M., Perry, J. M. G., Prevosti, F. J., Toledo, N., Cassini, G. H., & Fernicola, J. C. (2010). A baseline paleoecological study for the Santa Cruz Formation (late-early Miocene) at the Atlantic coast of Patagonia, Argentina. *Palaeogeography, Palaeoclimatology, Palaeoecology*, 292, 507–519. <https://doi.org/10.1016/j.palaeo.2010.04.022>
- Voss, R. S., & Jansa, S. A. (2003). Phylogenetic studied on didelphis marsupials II. Nonmolecular data and new IRBP sequences: Separate and combined analyses of didelphine relationships with denser taxon sampling. *Bulletin of the American Museum of Natural History*, 276, 1–82. [https://doi.org/10.1206/0003-0090\(2003\)276%3c0001:PSODMI%3e2.0.CO;2](https://doi.org/10.1206/0003-0090(2003)276%3c0001:PSODMI%3e2.0.CO;2)
- Voss, R. S., & Jansa, S. A. (2009). Phylogenetic relationships and classification of didelphid marsupials, an extant radiation of the new world metatherian mammals. *Bulletin of the American Museum of Natural History*, 322, 1–177. <https://doi.org/10.7934/p216>
- Vucetich, M. G., Kramarz, A. G., & Candela, A. M. (2010). Colhuehuapian rodents from Gran Barranca and other Patagonian localities: The state of the art. In R. H. Madden, A. A. Carlini, M. G. Vucetich, & R. F. Kay (Eds.), *The Paleontology of Gran Barranca: Evolution and Environmental Change through the Middle Cenozoic of Patagonia* (pp. 206–219). Cambridge University Press.
- Watson, A. G. (1981). The phylogeny and development of the occipito-atlas-axis complex in the dog. [Doctoral dissertation, Cornell University].
- Watson, A. G., de Lahunta, A., & Evans, H. E. (1989). Dorsal notch of foramen magnum due to incomplete ossification of supraoccipital bone in dogs. *Journal of Small Animal Practice*, 30, 666–673. <https://doi.org/10.1111/j.1748-5827.1989.tb01911.x>
- Weisbecker, V., Rowe, T., Wroe, S., Macrini, T. E., Garland, K. L. S., Travouillon, K. J., Black, K., Archer, M., Hand, S. J., Berlin, J. C., Beck, R. M. D., Ladevèze, S., Sharp, A. C., Mardon, K., & Sherratt, E. (2021). Global elongation and high shape flexibility as an evolutionary hypothesis of accommodating mammalian brains into skulls. *Evolution*, 75, 625–640. <https://doi.org/10.1111/evo.14163>
- Westerhold, T., Marwan, N., Drury, A. J., Liebrand, D., Agnini, C., Anagnostou, E., Barnett, J. K., Bohaty, S. M., de Vleeschouwer, D., Florindo, F., Frederichs, T., Hodell, D., Holbourn, A. E., Kroon, D., Laurentino, V., Littler, K., Lourens, L. J., Lyle, M., Pälike, H., ... Zachos, J. C. (2020). An astronomically dated record of Earth's climate and its predictability over the last 66 million years. *Science*, 369, 1383–1387. <https://doi.org/10.1126/science.aba6853>
- Wible, J. R. (2003). On the cranial osteology of the short-tailed opossum *Monodelphis brevicaudata* (Didelphidae, Marsupialia). *Annals of Carnegie Museum*, 72(3), 137–202. <https://doi.org/10.5962/p.316087>
- Wible, J. R. (2008). On the cranial osteology of the Hispaniolan solenodon, *Solenodon paradoxus* Brandt, 1833 (Mammalia, Lipotyphla, Solenodontidae). *Annals of Carnegie Museum*, 77(3), 231–402. <https://doi.org/10.2992/0097-4463-77.3.321>
- Wible, J. R. (2022). Ct study of the cranial osteology of the short-tailed opossum *Monodelphis domestica* (Wagner, 1842) (Marsupialia, Didelphidae) and comments on the internal nasal skeleton floor. *Annals of Carnegie Museum*, 87(4), 249–289. <https://doi.org/10.2992/007.087.0401>
- Wible, J. R., & Gaudin, T. J. (2004). On the cranial osteology of the yellow armadillo *Euphractus sexcinctus* (Dasypodidae, Xenarthra, Placentalia). *Annals of Carnegie Museum*, 73(3), 117–196. <https://doi.org/10.5962/p.316081>
- Wroe, S., Myers, T., Seebacher, F., Kear, B., Gillespie, A., Crowther, M., & Salisbury, S. (2003). An alternative method for predicting body mass: The case of the Pleistocene marsupial lion. *Paleobiology*, 29(3), 403–411. [https://doi.org/10.1666/0094-8373\(2003\)029%3c0403:AAMFPB%3e2.0.CO;2](https://doi.org/10.1666/0094-8373(2003)029%3c0403:AAMFPB%3e2.0.CO;2)
- Zachos, J., Pagani, M., Sloan, L., Thomas, E., & Billups, K. (2001). Trends, rhythms, and aberrations in global climate 65 Ma to present. *Science*, 292, 686–693. <https://doi.org/10.1126/science.1059412>
- Zimic, N. (2014). Avoiding competition: The ecological history of Late Cenozoic metatherian carnivores in South America. *Journal of Mammalian Evolution*, 21(1), 383–393. <https://doi.org/10.1007/s10914-014-8255-8>

## Publisher's Note

Springer Nature remains neutral with regard to jurisdictional claims in published maps and institutional affiliations.